Phyllosilicate Decomposition on Bennu Due to Prolonged Surface Exposure

Romy D. Hanna[1*], Victoria E. Hamilton[2], Chris H. Haberle[3], Hannah H. Kaplan[4], Cateline Lantz[5], Phil R. Christensen[6], Amy A. Simon[4], Dennis C. Reuter[4]

[1]Jackson School of Geoscience, University of Texas at Austin, TX 78712
[2]Southwest Research Institute, Boulder, CO
[3]Dept. Astronomy and Planetary Sci., Northern Arizona Univ., Flagstaff, AZ
[4]NASA Goddard Space Flight Center, Greenbelt, MD
[5]Université Paris Saclay, CNRS, Institut d'Astrophysique Spatiale, 91405, Orsay
[6]Arizona State University, Tempe, AZ USA

*Corresponding author (romy@jsg.utexas.edu)

Abstract

The Origins, Spectral Interpretation, Resource Identification, and Security–Regolith Explorer (OSIRIS-REx) mission to carbonaceous asteroid (101955) Bennu performed detailed mapping with a suite of instruments to characterize the composition and geology of its surface. Here we use data from the OSIRIS-REx Thermal Emission Spectrometer (OTES) instrument to investigate the relationship of OTES-derived spectral indices to other derived data products from OTES, the OSIRIS-REx Camera Suite (OCAMS), and the OSIRIS-REx Visible and InfraRed Spectrometer (OVIRS) at global and local scales. We quantitatively confirm that high values of the OTES silicate stretching slope (from ~10 to ~12 µm) in midday spectra that are indicative of thin and/or patchy dust cover are strongly associated with low thermal inertia (high porosity), low albedo boulders on Bennu. These high porosity boulders have brecciated textures with embedded clasts that likely originated on Bennu's parent body or during its disruption. The high porosity of these boulders is a key factor in the local production of the dust or its entrapment, as some large, brecciated boulders with a lower porosity have little evidence of dust. A second OTES spectral parameter, the silicate bending band depth near 22.7 µm applied to early evening spectra, is not correlated to thermal inertia, but is weakly to strongly correlated to albedo, OVIRS-derived 1.05 µm and 2.74 µm band depths, OVIRS-derived hydrogen abundance, and modeled nanophase troilite abundance. In several regions on Bennu there is a strong spatial relationship between these parameters, whereby areas with shallower silicate bending bands also have shallower 1.05 µm and 2.74 µm bands and lower albedo with higher nanophase troilite abundances. These correlations, combined with analysis of the silicate bending band in laboratory experiments of space weathered and mildly heated carbonaceous chondrites, suggests that decreased silicate bending band depths signify decomposition of phyllosilicates, likely Fe-bearing, due to space weathering or mild heating (<600 °C) via solar radiation during Bennu's time in near-Earth space. There is a strong association of larger silicate bending band depths in areas dominated by small rocks and unresolved material and in areas with small (≤ 25 m) craters identified as the spectrally reddest on Bennu, suggesting that this material has been more recently exposed due to impact and/or mass wasting processes. The shallowest silicate bending depths are associated with larger rocks and boulders that appear to have the longest surface exposure history, although there is band

depth variation among them suggesting either initial composition variation that resulted in different responses to space weathering or heating, or varied exposure history of individual boulders themselves. We predict that any grains returned from Bennu with a significant surface exposure history will be characterized by shallower 22.7 µm, 1.05 µm and 2.7 µm band depths and increased sulfide (troilite) abundance, as well as textural and chemical evidence for phyllosilicate dehydration.

Keywords: Asteroids, surfaces; Asteroids, composition; Asteroids, evolution; Regoliths; Spectroscopy; Solar Wind; Solar radiation

Highlights:

- Spectral evidence suggests phyllosilicate decomposition and dehydration has occurred on Bennu
- This phyllosilicate decomposition appears to be related to the surface exposure age of the material
- Phyllosilicate decomposition on Bennu is most likely caused by space weathering or mild solar radiative heating (<600 °C)

1. Introduction

As of this writing, the Origins, Spectral Interpretation, Resource Identification, and Security–Regolith Explorer (OSIRIS-REx) mission to carbonaceous asteroid (101955) Bennu is on its way back to Earth with a substantial cache (250 ± 150 g) of collected asteroid regolith (Lauretta et al., 2022). Prior to the collection event on October 20, 2020, the OSIRIS-REx spacecraft spent nearly two years characterizing the ~500-m-diameter rubble-pile asteroid with a large suite of instruments. During that time extensive imaging and mapping of Bennu's surface was done at a range of wavelengths, from the near infrared (NIR) through the far infrared (FIR), at a variety of spatial scales on the surface. From this rich dataset it was determined that the surface composition was most consistent with carbonaceous chondrites that are significantly hydrated, carbonate- and organic-bearing (CI/CM/C2; (Hamilton et al., 2019; Simon et al., 2020b)) and the presence of centimeters-thick, meter-long carbonate veins suggest extensive fluid flow on Bennu's parent body (Kaplan et al., 2020b). The surface was found to be surprisingly rough and boulder-rich, with only minimal exposures of small pebbles and grains that made sample site selection a challenge (Lauretta et al., 2019a; Lauretta et al., 2021). It was also found to be a relatively young and active surface with evidence for mass wasting and movement (Walsh et al., 2019; Jawin et al., 2020; Jawin et al., 2022), thermally-driven fracturing and exfoliation (Molaro et al., 2020a; Molaro et al., 2020b; Delbo et al., 2022), and regular ejection of (sub)centimeter-sized particles from the surface (Lauretta et al., 2019b; Hergenrother et al., 2020). Despite this recent surface activity several relatively old features are preserved including large craters on Bennu's equatorial ridge that likely formed during Bennu's time in the main belt up to 1 Gyr ago (Walsh et al., 2019) and boulder surfaces that likely record the totality of Bennu's residence time in near Earth space, 1.75 ± 0.75 Myr (Ballouz et al., 2020).

Further in-depth analysis of spectral datasets from the OSIRIS-REx Thermal Emission Spectrometer (OTES) and OSIRIS-REx Visible and InfraRed Spectrometer (OVIRS) instruments have yielded detailed insights into Bennu's surface composition and geologic history. Simon et al. (2020a) identified minor OVIRS bands consistent with phyllosilicate that correlate to the 2.74 µm hydration band on Bennu. Praet et al. (2021) estimated the mean hydrogen content through analysis of the 2.74 µm band and found that it was consistent with some aqueously altered chondrites (CM, C2) but not the most aqueously altered group (CI). Other studies have likewise suggested Bennu's spectra is a most consistent with a low petrologic type CM, CR, or ungrouped C2 chondrite, or some combination thereof, and likely represents a unique chondrite composition that is not present in our current meteorite collection (Merlin et al., 2021; Hamilton et al., 2022). Other analyses have suggested evidence for space weathering of Bennu's surface material that has further modified whatever initial lithology(ies) are present (Brunetto et al., 2020; DellaGiustina et al., 2020; Lantz et al., 2020; Trang et al., 2021; Clark et al., 2023).

One analysis thus far missing is a thorough integration of all available spectral datasets to gain a more integrated view Bennu's composition and geologic history. Analysis of OTES data suggest that this spectral dataset reveals little compositional variation on Bennu's surface, and is dominated, especially in the silicate stretching region, by transparency features associated with very thin and/or patchy dust (<5-10 µm in thickness) that is covering some of Bennu's surface (Hamilton et al., 2021) (Fig. 1). Those authors define within the daytime (12:30 pm local standard time, LST) OTES data a surface Type 1 and Type 2, with the latter containing more spectral evidence for dust presence (although minimal; thermal inertia data of Bennu does not require dust to be present but places an upper limit of <50 µm thickness, consistent with the spectral data (Rozitis et al., 2020)). However, other analysis of the OTES data hint that some further information regarding composition or space weathering effects can be obtained from this dataset (Lantz et al., 2020; Breitenfeld et al., 2022).

Here we investigate the OTES surface Types 1 and 2 of Hamilton et al. (2021) and other OTES spectral indices that utilize the two major bands present in OTES data – the silicate stretching and bending bands (Fig. 1). We compare these indices to numerous other spectral indices defined by the OVIRS and OSIRIS-REx Camera Suite (OCAMS) instruments, using both globally quantitative and a more localized, detailed analysis approach. For the latter we explore the geomorphologic setting of the various spectral datasets through OCAMS visible imagery to further understand the geologic setting and relationship of the various spectral units.

2. Methods

We used data and derived data products from the OTES, OVIRS, and OCAMS instruments (Table 1). The OTES instrument is a hyperspectral point spectrometer that measures emitted radiance from 1750 to 100 cm^{-1} (5.71 to 100 µm) with an 8-mrad diameter field of view. Details on OTES instrument calibration, performance, and data processing can be found in Christensen et al. (2018b; 2019) and Hamilton et al. (2019; 2021). The OVIRS instrument is a visible to near infrared point spectrometer that measures reflected radiance over 0.4–4.3 µm (25,000–2300

cm^{-1}) with a 4-mrad diameter field of view. OVIRS instrument calibration, performance, and data processing details are in Reuter et al. (2018) and Simon et al. (2018). The OCAMS consists of three cameras, SamCam, MapCam, and PolyCam, that are used to image the surface of Bennu at multiple spatial scales and visible wavelengths (Rizk et al., 2018).

We utilized OTES spectral data collected during the Detailed Survey (DS) mission phase, primarily from Equatorial stations 3 (EQ3; 12:30 pm local solar time (LST)) and 6 (EQ6; 8:40 pm LST), as these represented the daytime and nighttime spectra with the highest signal to noise ratio (SNR). While the EQ6 data may not show the least radiance contribution from the dust that is known to be present on Bennu's surface compared to other nighttime spectra, it has higher SNR for spectral analysis than the pre-dawn data while still having a significantly reduced dust contribution (Hamilton et al., 2021). We explore the possible dust radiance contribution from this early evening local solar time when analyzing the EQ6 data.

OTES spectra were selected to be fully on-body (FOV fill flag = 1) with a mean emission angle less than 55 degrees and radiometric quality 0 to 2 (meaning space observations were used for calibration and no phase inversions are present in the spectra (Christensen et al., 2019a)). The Si-O silicate stretching ratio (SR) and Si-O bending band depth (BBD) spectral indices are calculated the same as in (Hamilton et al., 2021). The SR and BBD were called the R987/814 and BD440 in that work, but because these numbers refer to wavenumbers and we compare to OVIRS and OCAMS datasets that reference wavelength, we rename them here to avoid confusion. For SR, the average emissivity for OTES channels 113-115 (~996 - 978 cm^{-1}; 10.0 – 10.2 µm) is divided by the average of channels 93-95 (~823 - 805 cm^{-1}; 12.2 – 12.4 µm). For BBD, the average emissivity of channels 60-62 (~537 - 520 cm^{-1}; 18.6 – 19.2 µm) plus the average emissivity of channels 43-45 (~390 - 372 cm^{-1}; 25.6 – 26.9 µm) is divided by two and then divided by the average emissivity in channels 50-51 (~442 - 433 cm^{-1}; 22.6 – 23.1 µm). For the Si-O stretching band depth (SBD) we neglected the Christiansen frequency region (~1120-1090 cm^{-1}; 9.0 – 9.2 µm) because of higher noise in this area, especially during the EQ6 (8:40 pm) station due to colder surface temperatures. Therefore, SBD was calculated as the average emissivity of channels 67-69 (598-580 cm^{-1}; 16.7-17.2 µm) divided by the average emissivity of channels 104-108 (935-901 cm^{-1}; 10.7 – 11.1 µm). Errors for all indices were calculated using the standard error for each channel average and propagating it according to the math formula of the index.

In order to test for global correlations between spectral parameters on Bennu that have been acquired at different times and/or with different instruments, the various spectral indices were mapped onto the 50k faceted shape model of Barnouin et al. (2019). For the SBD global map created for this work, values were combined using the weighted average algorithm of Ferrone et al. (2021). All SR and BBD global maps (also mapped onto the 50K Bennu shape model) are from Hamilton et al. (2021).

All other global, faceted spectral maps used in this work are also mapped using the 50K Bennu shape model and are described in previous works. The OVIRS-derived bond albedo map is from Li et al. (2021), the OTES-derived thermal inertia map is from Rozitis et al. (2020), and the OVIRS

2.74 band depth map is from Simon et al. (2020b). We used the modeled space weathering maps from OVIRS data from Trang et al. (2021) and the four OCAMS-derived spectral maps of DellaGiustina et al. (2020): normal reflectance at 0.55 µm, normalized 0.85/0.55 µm visible slope proxy, normalized 0.47/0.55 µm near-UV slope proxy, and relative band strength at 0.7 µm. Because the OCAMS images used to generate the global maps had a per pixel resolution of ~25 cm (DellaGiustina et al., 2020), all OCAMS maps were blurred to approximate the OTES resolution (~40 m) using a Gaussian convolution kernel (see Rozitis et al. (2020) for details). We used the two hydrogen abundance maps of Praet et al. (2021) (the effective single-particle absorption thickness (ESPAT) and normalized optical path length (NOPL) maps) as additional hydration index maps and also investigated seven other OVIRS-derived spectral parameters (0.55 µm band, 1.05 µm band, 1.4 µm band, 1.8 µm band, 2.3 µm band, spectral slope from 0.5 to 1.5 µm, and band area from 3.2 to 3.6 µm) (Kaplan et al., 2020a; Simon et al., 2020a; Simon et al., 2020b).

To test for correlations between various datasets we followed the method of Simon et al. (2020b) and calculated the Spearman's rank correlation coefficient. We selected this parameter to test for a relationship between datasets as it requires only a monotonic relationship, and not necessarily a linear one, between two variables. We interpret a strong correlation as $r > 0.6$, moderate correlation as $r = 0.5 – 0.59$, and weak correlation as $r = 0.4 – 0.49$. A correlation value less than 0.40 is interpreted as a non-significant correlation in this work. To account for the error for each dataset (which vary depending on the instrument used, observation details, and the calculation method of each dataset) in the Spearman's rank correlation test we used the Monte Carlo perturbation method described by Curran (2014). The Spearman's rank correlation (r) reported herein is the average and 1 standard deviation of rank correlation values of 20k simulations using the dataset's reported error as the 1 sigma error. All correlation results are reported in Table S2.

We used the J-Asteroid program, a variant of JMARS (Christensen et al., 2009; Christensen et al., 2018a), to visualize the mapped spectral datasets along with OCAMS visible imagery to assess their spatial relationships, geomorphology and surface textures. We used a photometrically corrected, global, 5 cm/pixel OCAMS PolyCam mosaic as a visible basemap of Bennu's surface (Bennett et al., 2021), and individual PolyCam images for higher resolution investigations of local sites.

Here we also report previously unpublished spectral results from a study on experimental heating of highly altered CM 2.1 ALH 83100 (Lindgren et al., 2020). Similar to the other chips that were heated for that study, a chip (123 mg) of ALH 83100 was placed in a platinum crucible and heated in a tube furnace under vacuum (~5 x 10^3 mbar), and in this case held at 400 °C for a full week. After heating the chip was embedded in resin, sectioned, and polished. Infrared reflectance spectra on the polished section were acquired using a Thermo Scientific iN10 FTIR microscope (µ-FTIR) equipped with an extended range, liquid nitrogen–cooled mercury cadmium telluride (MCT) detector, and potassium bromide (KBr) beamsplitter. Spectra were collected as a map over the section with an individual spot size of 300 µm per pixel and an average of 256 scans with a 2 cm^{-1} spectral sampling over 4000–400 cm^{-1} (2.5–25 µm). Spectra were averaged (n =28) to create an average spectrum of the heated chip and plotted as emissivity (assuming Kirchhoff's Law, E = 1-R, is sufficiently applicable, where E is the emissivity and R is the reflectance; (Salisbury, 1993)). Further details on experimental and spectral measurements and data processing, including for the previously published unheated and 24-hour heated chip data, can be found in Lindgren et al. (2020).

3. Results

3.1 OTES Spectral Parameters and Global Correlations

First we revisit the relationship between the silicate stretching ratio (SR) at 10.0 – 12.4 µm (~996 - 805 cm^{-1}) which is used to define the two spectral Types 1 and 2 (relatively lower and higher dust, respectively) of Hamilton et al. (2021), and the silicate bending band depth (BBD) at 22.7 µm (440 cm^{-1}), which is also influenced by the presence of the dust (Graff, 2003) (Fig. 1). During the day (EQ3) when radiance of the dust contributes significantly to the spectral signature of the surface measured by OTES, there is a moderate negative correlation (r = -0.53 (0.05)) between these spectral parameters. This correlation in the daytime data disappears at night (EQ6; 8:40 pm LST; r = -0.13 (0.02)) when dust radiance is reduced (Fig. 2a-b). As noted by Hamilton et al. (2021), this moderate (but not strong) correlation during the day suggests that there is one or more factors other than the dust presence influencing these bands, which could include variability among spectra in SNR and anisothermality. When these same spectral parameters are calculated as a weighted average on each facet of the Bennu shape model, the Spearman's rank correlation values are higher but the interpretation remains the same: the dust radiance during the day results in a strong correlation (r = -0.75 (0.04)) between the SR and the BBD, which is then absent (r = -0.28 (0.05)) at night (Fig. 2c-d). It is not clear why the Spearman's rank correlation values are higher when averaging the spectral parameters over a global faceted map, but it could be due to noise reduction through the averaging of several OTES spots per facet, or a smearing effect that occurs when mapping partially overlapping OTES spots that are much larger (~40 m) than the ~5 m facet (Ferrone et al., 2021).

We next examined the relationship between the SR and OVIRS-derived bond albedo (Li et al., 2021) and OTES-derived thermal inertia (Rozitis et al., 2020). During the day, the SR shows a strong negative correlation with albedo (r = -0.65 (0.04)) and thermal inertia (r = -0.63 (0.02)) (Fig. 3a,c). However, these correlations are not present when using the nighttime OTES spectra (both r < 0.40) when the spectral radiance of the dust is low (Fig. 3b,d). This quantitatively confirms the inference of Hamilton et al. (2021) that the presence of the dust (e.g., Type 2, high dust surface) is primarily associated with low albedo, low thermal inertia surfaces on Bennu. It is important to note that the low thermal inertia of the surface is not primarily due to the presence of the dust but rather reveals a physical property of the underlying rock, which has been interpreted as high porosity (Rozitis et al., 2020). The dust cover is too thin and/or patchy (5-10 µm; (Hamilton et al., 2021)) to significantly contribute to the thermal signature of the surface that is a function of the thermal skin depth, which is a few centimeters on Bennu (Rozitis et al., 2020).

The relationship between the BBD and the OVIRS bond albedo and OTES thermal inertia are also shown in Figure 3. The daytime BBD has a strong positive correlation (r = 0.64 (0.03)) to albedo and a moderate correlation to thermal inertia (r = 0.51 (0.03)). The nighttime BBD has no correlation with thermal inertia (r = 0.17 (0.05)) but is still correlated to albedo 0.59 (0.06)). This is significantly different behavior than that observed for the SR (aka Type 1/2) that is strongly influenced by the presence of dust and not correlated with either albedo or thermal inertia at night when dust radiance is minimized (Fig. 3b,d). This suggests that the nighttime EQ6 BBD is influenced by something other than (or in addition to) the presence of dust. However, if this non-dust factor is also contributing to the BBD during the day, this may also explain the only moderate correlation (r = -0.53 (0.05)) between the SR and the BBD EQ3 daytime data on a per-OTES spectrum basis (Fig. 2a). Whatever is controlling the nighttime BBD, it appears to be correlated with variations in albedo. Specifically, the smallest BBDs are associated with lower albedo surfaces.

We also examined the relationship of the Si-O stretching band depth (SBD) to the BBD and find that they are strongly positively correlated (r = 0.80 (0.04)) during the day and moderately correlated (r = 0.52 (0.05)) at night (Fig. 4a,b). The strong daytime correlation is most likely due to presence of the dust, which will decrease the depth of both the Si-O stretching and bending bands in tandem (Graff, 2003, see also Hamilton et al. 2001), but at night, when dust radiance is assumed to be minimal, another explanation is required. Two possibilities could explain the moderately correlated band depths at night: 1) dust is still contributing the radiance at this time of day (8:40 pm); or 2) small particle size or surface roughness variations (at the scale of OTES wavelengths) on Bennu's surface is decreasing spectral emissivity contrast across all wavelengths (Vincent and Hunt, 1968; Ramsey and Christensen, 1998; Ramsey and Fink, 1999; Osterloo et al., 2012).

However, comparing the silicate stretching and bending band depths of the individual OTES spectra reveals that the band depths are in fact not correlated at night (r = 0.28 (0.04); Fig. 4D), suggesting again that correlation values from global, faceted map data can be higher due to the averaging or smearing of the large OTES spots onto the smaller map facets, likely masking heterogeneity present at smaller spatial scales. The strong correlation (r = 0.63 (0.04); Fig. 4C) of the individual daytime band depths is readily explained by the presence of dust, but the lack of correlation at night suggests that neither dust radiance, nor spectral contrast differences due to variations in particle size or surface roughness, can account for all of the variation of the nighttime BBD across Bennu's surface. A particle size effect is also inconsistent with the positive correlation of the nighttime BBD to albedo. If a smaller particle size was causing decreased BBD (e.g., Vincent and Hunt, 1968), we would expect increased visible albedo with smaller particle sizes (e.g., Cloutis et al., 2011b), but we see the opposite trend (Fig. 3f).

Spectral averages of the 300 nighttime EQ6 spectra with the with smallest and largest BBDs also suggest minimal radiance contribution from dust (Fig. 5). The small and large BBD spectra both show a silicate stretching shape in the ~1100-700 cm^{-1} (~9-14 µm) spectral region that is very similar to the lowest dust (Type 1) spectrum. To further confirm that there is minimal dust contribution in the EQ6 8:40 pm data, we examined the SR and BBD of average OTES spectra among all seven equatorial stations for eight individual sites on Bennu (Supplemental Material). We find that there is no measurable difference or discernable trend in BBD between day and night observations for any of the sites, including the high dust, Type 2 sites. This strongly suggests that compared to the SR, the BBD is a less sensitive indicator of the presence of dust on Bennu, regardless of the time of day, and dust is not contributing significantly to the EQ6 nighttime BBD. We therefore rule out dust radiance, in addition to particle size/surface roughness variations, as explaining the majority of the variation in the nighttime BBD across the surface of Bennu.

Finally, we examine the global, spatial relationship between the surfaces defined by the daytime EQ3 SR (Types 1 and 2, low and high dust, respectively) of Hamilton et al. (2021) and surfaces defined by nighttime EQ6 BBD (Fig. 5B, 6). Comparing these indices at the global, faceted map scale indicate that dusty, Type 2 surfaces tend to have lower EQ6 BBD (r = -0.54 (0.05); Fig. 5b), suggesting they are in fact the same surface (i.e., they are co-located) even though the EQ6 BBD is not indicative of dust (for most of Bennu's surface; see above and Supplemental Material). However, we have already shown that using global, faceted maps may cause correlations to appear higher due to averaging and/or spatial smearing of the OTES spectral spots (Figs 2, 4), and so this correlation may not be as strong as indicated. And the relationship of the different OTES spectral surfaces with OTES thermal inertia suggests they are not the same surface. While Type 2 (dusty) surfaces are correlated to OTES thermal inertia (r = -0.63 (0.02); Fig. 3c), surfaces defined by the EQ6 BBD are not (r = 0.17 (0.05); Fig. 3h). If these spectral surface types represent the same surface on Bennu then EQ6 BBD surfaces should be positively correlated to OTES thermal inertia as well, but they clearly are not (Fig. 3h). The global maps of OTES spectral Types 1/2 and EQ6 BBD also show that the maps are not simple inverses of each other, although there are several areas that are characterized as both a strong Type 2 (i.e., dusty) surface with a very low EQ6 BBD (Fig. 6). In the following sections we compare these OTES spectral surface types (EQ3 SR Type 1/2 representing dust-free/dusty surfaces, and surfaces defined by their EQ6 BBD) to other OVIRS- and OCAMS-derived spectral indices, first at the global, faceted map scale, and then at localized scales.

3.2 Global correlations of OTES spectral surfaces with other spectral parameters

We determined if either of these two OTES spectral indices (EQ3 SR (e.g. Type 1/2) and EQ6 BBD) are correlated to any other spectral indices that have been calculated and mapped globally for Bennu. For space weathering indices of Bennu, we used the modeled space weathering maps from OVIRS data from Trang et al. (2021). We checked for correlations using all maps from this work: nanophase and microphase iron, troilite, and magnetite abundance. The only correlations present (r > 0.40) are for nanophase troilite, which has a moderate positive correlation with both the daytime EQ3 SR (r = 0.45 (0.07)) and the EQ6 BBD (r = -0.44 (0.09)) (Fig. 7a,b). We also checked for correlations between four OCAMS-derived spectral maps of DellaGiustina et al. (2020): normal reflectance at 0.55 µm, normalized 0.85/0.55 µm visible slope proxy, normalized 0.47/0.55 µm near-UV slope proxy, and relative band strength at 0.7 µm. The only correlations identified were for the EQ3 SR (r = -0.77 (0.02)) and EQ6 BBD (r

= 0.51 (0.05)) to normalized reflectance at 0.55 µm (i.e., albedo; not shown), consistent with correlations found using the OVIRS-derived bond albedo (Fig. 3).

For comparison to hydration indices we used the 2.74 µm hydration band depth map of Simon et al. (2020b) and the two hydrogen abundance maps of Praet et al. (2021). For all three hydration indices, the EQ6 BBD is always more strongly correlated to hydration than the EQ3 SR (Fig. 7, S3). Results are most similar for the OVIRS 2.74 band depth and the effective single-particle absorption thickness (ESPAT) parameter, in which the EQ3 SR (i.e., dust) is not correlated ($r < 0.30$) to the hydration indices, but the EQ6 BBD is weakly ($r = 0.44(0.07)$ & 0.47 (0.08)) correlated. However, both OTES spectral parameters are weakly correlated to the normalized optical path length (NOPL) parameter ($r = -0.41$ (0.01) and $r = 0.48$ (0.06)). It is unclear why the NOPL parameter would show a correlation to EQ3 SR while the other two hydration indices do not, but Milliken and Mustard (2007) point out that this parameter increases exponentially with water content, while the ESPAT parameter increases only linearly. Because Bennu's surface is dominated by carbonaceous chondrite-like materials (Hamilton et al., 2019) that have relatively high water contents (> 5 wt. %; (Garenne et al., 2014)), the NOPL is likely a less sensitive indicator of hydration of Bennu's surface at these elevated water contents (see Milliken and Mustard (2007) Fig. 3). In other words, the NOPL parameter will have less variability across Bennu's surface, which is indeed the case (note differing scales of each parameter in Fig. S3 and see also Fig. 3 of Praet et al. (2021)). Regardless of hydration index, all results indicate that there is a weakly positive correlation between the EQ6 BBD and the apparent degree of hydration of Bennu's surface, but little to no correlation between the EQ3 SR (dust) and hydration. Finally, we checked for correlations of the EQ3 SR and EQ6 BBD to seven other OVIRS-derived spectral parameters (0.55 µm band, 1.05 µm band, 1.4 µm band, 1.8 µm band, 2.3 µm band, spectral slope from 0.5 to 1.5 µm, and band area from 3.2 to 3.6 µm) (Kaplan et al., 2020a; Simon et al., 2020a; Simon et al., 2020b) and found a correlation ($r > 0.40$) for only the 1.05 µm band with the EQ6 BBD ($r = 0.47$ (0.06); Fig. 7).

3.3 Spatial relationship and geological context of OTES spectral indices

As discussed above, spectral indices mapped onto global faceted maps of Bennu may result in higher correlations than may be present (see Figs. 2,4), due to the averaging of overlapping spots that are larger than the facet size. And it is apparent from global mapping that Bennu shows thermal, morphological and spectral heterogeneity at the ~5 m scale (e.g., DellaGiustina et al., 2020; Rozitis et al., 2020; Hamilton et al., 2021; Jawin et al., 2022) and so downgrading the resolution (i.e., increasing the facet size) of the spectral maps would further obfuscate any trends. Therefore, we examined several localized areas on Bennu, to determine the spatial relationship between, and geological context of, the two OTES spectral indices (Type 1/2 defined by EQ3 SR, and EQ6 BBD), focusing on the possible trends already identified at the global scale (thermal inertia, albedo, hydration, 1.05 µm band depth, troilite abundance). We examined several individual sites on Bennu but focus here on three areas that highlight the trends we observed on Bennu (Fig. 6). These areas include a highly dusty (high EQ3 SR) boulder (Roc Saxum; Fig. 8-9), a large boulder field that appears relatively dusty with low EQ6 BBD values (part of Tlanuwa Regio; Fig. 10-11), and an area with varied dust and EQ6 BBD values (centered on Bralgah crater; Fig. 12-14). Because all three OVIRS-derived hydration indices generally show the same trends with the OTES spectral indices, for simplicity we only mapped and analyzed the 2.74 band depth at the local scale. Likewise, we did not examine the OCAMS normalized reflectance at 0.55 µm as this parameter is a proxy for, and globally showed same trends as, OVIRS-derived bond albedo.

One of the most distinct Type 2 (dusty) areas is shown in Figure 8. It is a large (~70 m across), partially exposed boulder (Roc Saxum) that is characterized by low albedo and low thermal inertia, and as expected these two properties are strongly co-located with the highest EQ3 SR values. Unlike the EQ3 SR which is uniformly high across the boulder, the other mapped parameters (EQ6 BBD, 1.05 and 2.74 µm band depths, and troilite abundance) vary across the boulder surface. While the daytime EQ3 OTES data (in the SR region) is dominated by the radiance of the overlying dust, we know from our previous analyses that the EQ6 BBD has little contribution from dust radiance, and therefore is likely dominated by the spectral signature of the underlying boulder material. Further, the general trends of the EQ6 BBD, 1.05 and 2.74 µm band depths, and troilite abundance across the boulder are approximately spatially correlated – the northern part of the boulder is generally lower in EQ6 BBD and 1.05 and 2.74 µm band depths and higher in troilite abundance, compared to the southern portion of the boulder.

The surface texture of the boulder itself is relatively smooth, with numerous curvilinear fractures, some of which appear to be surrounding lithologically distinct clasts indicating that the boulder is a breccia (Fig. 9a). Some separate, small rocks appear to be lying on top of the boulder, but it is unclear whether these are clasts derived from the boulder itself, or were emplaced on the boulder due to mass movement of small rocks, as has been proposed for many of the large boulders on Bennu (Jawin et al., 2022). The area to the south of the boulder (white box in PolyCam mosaic of Fig. 8) is also spectrally distinct from both the boulder and the surrounding terrain, and has locally high EQ6 BBD, 1.05 and 2.74 µm band depths, and a lower troilite abundance. The EQ3 SR (dust abundance) is lower than that of the boulder but varies across the area. The albedo and thermal inertia of this area are both higher than the nearby boulder, and the area is dominated by small, bright rocks as well as unresolved material (Fig. 9b). In summary, for this area the EQ6 BBD index is not spatially correlated to the EQ3 SR dust index, and higher EQ6 BBD values are associated with larger 1.05 µm band depths, greater hydration (we use this term here, and for the rest of the manuscript, to mean the depth of the 2.74 band), and lower troilite abundance in areas dominated by smaller rocks and unresolved areas. The EQ3 SR dust index is not as spatially correlated at this local scale to 1.05 µm band depth, hydration or troilite abundance, but high values are strongly associated with low albedo and low thermal inertia, and is associated with a single, relatively coherent but brecciated boulder.

Another area characterized by a relatively higher amount of dust is a large boulder-rich region (Fig. 10). Here the highest EQ3 SR values are coincident with the densest proportion of large boulders. Thermal inertia and albedo values are somewhat lower than the surroundings but are not uniform over the highest EQ3 SR area, likely due to a mix of boulder sizes and types. And similar to the large boulder in Fig. 8, the dusty boulders show heterogeneity in EQ6 BBD, 1.05

and 2.74 µm band depths, and troilite abundance among them. The relatively small size of the boulders (< 20 m across) compared to the spot sizes of OVIRS (~20 m) and OTES (~40 m) data make co-locating these spectral signatures more precisely difficult, although one localized area with a lower EQ6 BBD, 1.05 µm band depth, and hydration, and higher troilite abundance is apparent (white arrow in Fig. 10). The boulder-free region to the southwest of this area is distinctly higher in albedo, EQ6 BBD, hydration, 1.05 µm band depth, and lower in troilite abundance, compared to the boulder-rich region.

Once again, areas with the highest EQ3 SR values are dominated by large boulders and rocks, many of which are obvious breccias (Fig. 11a,b), and within this boulder area is the lowest EQ6 BBD region, with relatively low 1.05 µm band depth and hydration and high troilite abundance (white arrow; Fig. 10). In contrast, the southwestern area, which is less dusty with higher EQ6 BBD, larger 1.05 µm band depth, higher hydration, and lower troilite, is dominated by smaller rocks as well as some unresolved areas (Fig. 11c). This transition in rock size between high and low EQ3 SR (dust) areas is well illustrated in Fig. 11b, which overlaps this boundary.

The final region contains large contiguous areas of high and low EQ6 BBD and EQ3 SR, but again they are not spatially collocated to a high degree (Fig. 12). While EQ6 BBD is less consistently spatially correlated with 1.05 µm band depth, hydration and troilite abundance than in the previous areas, the highest EQ6 BBD values do show relatively larger 1.05 µm band depth, moderate to high hydration and lower troilite abundance (yellow dashed area in Fig. 12). And conversely, two areas with the lowest EQ6 BBD values display relatively smaller 1.05 µm band depth, lower hydration and higher troilite abundance (white dashed areas in Fig. 12). And as seen elsewhere on Bennu, these three OVIRS spectral parameters are more spatially correlated to EQ6 BBD values than to EQ3 SR values. The PolyCam images over the three EQ6 BBD areas show familiar trends documented in the other areas. The high EQ6 BBD area is dominated by small rocks and unresolved areas (Fig. 13a), while the two areas with smaller BBD values contain larger, brecciated boulders (Fig. 13b,c).

One final interesting observation in this area is the presence of a large boulder in the southeast corner that has a distinctly low thermal inertia compared to other similarly-sized boulders in the region (white arrows Fig. 12). And, as expected, this boulder is also significantly more dusty than the other boulders, further supporting the hypothesis that low thermal inertia (i.e., high porosity (Rozitis et al., 2020)) boulders are locally producing and/or trapping dust, as originally proposed by (Hamilton et al., 2021) and quantitatively confirmed (Fig. 3) in this study. Comparing to the other boulders in the area, there are no other spectral parameters that make this boulder unique – it is only the dust signature and OTES thermal inertia. In particular, apart from these two properties, it looks spectrally similar to the boulder directly to the west (similar albedo, EQ6 BBD, 1.05 and 2.74 µm band depths, troilite abundance). Looking at these two boulders with PolyCam imagery (Fig. 13, 14) both boulders appear to be brecciated with embedded clasts, although the low thermal inertia boulder has obvious layering with one large, 2 meter-wide highly clastic layer (Fig. 14). But, the presence of layering does always result in low thermal inertia and dust, as the northern most boulder also has layering but higher thermal inertia with lower dust (Fig. 12, 13c). Therefore, whatever is causing the unusually high porosity, and thus dust cover, in some boulders on Bennu is not clear from our analysis here.

4. Discussion

4.1 Relationships of spectral parameters

Our results quantitatively confirm the hypothesis of Hamilton et al. (2021) that high EQ3 SR values, which are indicative of thin and/or patchy dust cover on Bennu, are correlated with low thermal inertia, low albedo surfaces. Global correlation tests using values mapped onto a 50k faceted shape model of Bennu show a strong correlation of EQ3 SR to OTES-derived thermal inertia (r = -0.63 (0.02)) and OVIRS-derived albedo (r = -0.65 (0.04)) (Fig. 3). These correlations are evident at local scales as well - in all three examined areas high EQ3 SR values are strongly spatially correlated to low thermal inertia, low albedo surfaces (Figs. 8, 10, 12). Further, all these areas are dominated by easily resolvable boulders that are brecciated with embedded clasts (Figs. 9a, 11b,11c, 14b, 14c). Layering is evident in some of these low thermal inertia boulders (Fig. 14b,c), although visible layers within the boulder does guarantee that the boulder has a strong dust (high EQ3 SR) signal (Fig. 13c). The strong association of dust with high porosity, brecciated rocks strongly suggests that the high porosity of the boulders is a key factor in the local production of the dust or its entrapment. This requirement of a relatively high porosity is especially illustrated by the region in Figure 12, where the only boulder with measurable dust cover has a significantly lower thermal inertia (i.e., high porosity).

Conversely, lower dust (low EQ3 SR) areas with higher albedo and thermal inertia are consistently dominated by smaller rocks and unresolved areas (Figs. 9b, 11b, 11c, 13a). The tendency of smaller rocks to have higher thermal inertia (i.e., lower porosity) was also noted by Cambioni et al. (2021). That study found an inverse correlation between porosity and the local abundance of sub-centimeter rocks and proposed that lower porosity boulders were much more efficient at breaking down into smaller rocks and regolith through impact and thermal fatigue. In contrast, high porosity boulders were less likely to be broken up into small rocks by thermal fatigue or impact, and were more likely to be compressed in situ, rather than fragmented. This reinforces the finding that porosity is key to dust production – lower porosity rocks (which are also more efficiently broken into smaller sizes) have less evidence of dust (i.e., have lower EQ3 SR values). It is only the larger, higher porosity boulders (that can remain large in size due to their higher porosity) that are locally producing and/or retaining the dust. Perhaps the same process that is compressing high porosity boulders in situ is producing or trapping the dust. Alternatively, Jawin et al. (2022) proposed that dust is entrapped on dusty boulders during mass movement and boulder excavation, but if this is true, boulder porosity still appears to be a key factor in trapping the dust. The original source of the high porosity within large boulders on Bennu is even more speculative, but it is likely a pre-Bennu signature (i.e., original accretionary porosity, or related to activity on Bennu's parent body or formed during its disruption), as such brecciated and layered textures could not be formed on relatively quiescent, present-day Bennu.

The other OTES spectral index examined in this work, EQ6 BBD, does not have a correlation to OTES-derived thermal inertia (r = 0.17 (0.05)), but is correlated to OVIRS-derived albedo (r = 0.59 (0.06)). And although global, faceted map-based analysis suggests a correlation of EQ6 BBD to dust presence (EQ3 SR; r = -0.54 (0.05); Fig. 5), this correlation is revealed to be rather weak when examining localized areas on Bennu (Figs. 6, 8, 10, 12). Specifically, we document several areas where large, dusty boulders have either a varied EQ6 BBD signature across it (Fig. 8) or among the boulders themselves (Fig. 10). And in the last area, two boulders with similar EQ6 BBD values have markedly different amounts of dust (EQ3 SR values; Fig. 12). Further, our analysis revealed there is no significant dust radiance contributing to the EQ6 BBD spectral index.

When comparing the EQ3 SR and EQ6 BBD to various OCAMS- and OVIRS-derived spectral indices at the global scale, we find weak to moderate correlations of EQ6 BBD to the 1.05 µm band depth (Simon et al., 2020a), hydration indices (2.74 µm band depth, NOPL, ESPAT (Kaplan et al., 2020a; Praet et al., 2021)) and one space weathering spectral index, nanophase troilite abundance (Trang et al., 2021) (Fig. 7, S3). While the EQ3 SR is also weakly correlated to nanophase troilite and NOPL, the EQ6 BBD has a higher correlation value, including error, to both indices (Fig. 7, S3). On a localized scale, the different relationships of these indices become clearer. In the three regions examined, EQ6 BBD has a much stronger spatial correlation to 1.05 µm band depth, hydration (2.74 µm band depth) and troilite abundance compared to the EQ3 SR (Figs. 8, 10, 12). Specifically, areas with the lowest EQ6 BBD values have consistently smaller 1.05 µm band depths and are relatively lower in hydration and higher in troilite abundance. Conversely, areas with the highest EQ6 BBD values have relatively larger 1.05 µm band depths with a stronger hydration signature and lower troilite abundance. Further, we find the 1.05 µm band depth is globally correlated to both the 2.74 µm band depth (r = 0.48 (0.02); not shown – all further correlation values are not plotted but values are listed in Table S2) and troilite abundance (r = -0.50 (0.10)). Troilite abundance and 2.74 µm band depth are not correlated at the global, faceted-map scale (r = -0.37 (0.10)), however. We note that the correlations of the EQ6 BBD to various OVIRS-derived spectral parameters further supports that the BBD is largely indicative of lithologic (compositional) variation, and not due to particle size, surface roughness or texture effects.

In summary, while not a consistent global trend, for the localized regions examined here, areas with low BBD values on Bennu are associated with decreased hydration, smaller 1.05 µm band depths, increased nanophase troilite abundance, and low albedo..

4.2 Space weathering or mild heating on Bennu

The trend of decreased hydration, EQ6 BBD, and albedo with increased troilite abundance on Bennu could be indicative of either space weathering or mild heating. Laboratory experiments and spacecraft observations consistently show that both a decrease in hydration and increase in sulfide abundance (including troilite) occur in the course of space weathering of carbonaceous chondrite meteorites and asteroids (Matsuoka et al., 2015; Thompson et al., 2019; Matsuoka et al., 2020; Thompson et al., 2020; Trang et al., 2021; Noguchi et al., 2022).

Multiple laboratory experiments also exhibit visible to near-infrared (0.5 – 2.5 µm) spectral darkening (i.e., decrease in albedo) with space weathering of carbonaceous chondrites and phyllosilicates (the dominant mineral in hydrated carbonaceous chondrites) (Matsuoka et al., 2015; Matsuoka et al., 2020; Thompson et al., 2020; Prince and Loeffler, 2022; Zhang et al., 2022). Likewise, multiple studies of heated carbonaceous chondrite material show that mild heating results not only in dehydration but also in sulfide formation, including troilite (Tonui et al., 2014; Lindgren et al., 2020; King et al., 2021) and decreased reflectance (visible albedo) (Cloutis et al., 2012; Lindgren et al., 2020; Matsuoka et al., 2022). Mild heating in this case refers to temperatures below the ~600°C threshold at which point phyllosilicates have completely broken down and the 3-micron band is no longer detectable (Mogi et al., 2017; Nakamura et al., 2017; King et al., 2021; Matsuoka et al., 2022). Globally on Bennu there is a strong correlation of both lower hydration (OVIRS 2.74 µm band depth r = 0.60 (0.07)) and higher troilite abundance (r = -0.61 (0.05)) with lower albedo. Therefore, the correlation of OVIRS spectral indices in regard to hydration, albedo, and troilite abundance are consistent with space weathering or mild heating of carbonaceous chondrite material on Bennu.

Fewer studies have examined the effect of space weathering or mild heating in the mid- to far-infrared wavelength range covered by OTES. The single study on space weathering of carbonaceous chondrites that included the silicate bending wavelength region indicates that space weathering decreases the BBD relative to the Si-O stretching band depth in CM-type carbonaceous chondrites (Brunetto et al., 2020) (Fig. 15). For CI Alais, the relative band depths of the silicate stretching and bending bands remained unchanged, and for ungrouped C2 Tagish Lake the BBD increased relative to the silicate stretching band depth after irradiation (Fig. 15). These differences in irradiation response in the BBD could be related to phyllosilicate compositional differences as this band is a combination of three overlapping bands – the Si-O bending band, the Mg-O-Si deformation band, and the Fe-O-Si deformation band – that arise from the phyllosilicates that are volumetrically dominant in hydrated carbonaceous chondrites (Hanna et al., 2020 and references therein). CMs have a distinctly different phyllosilicate chemistry compared to CIs and C2 Tagish Lake, with significantly higher proportions of Fe (Zolensky et al., 1993; Zolensky et al., 2002). Therefore, the decreased BBD in space-weathered CM chondrites could be related to the destruction of Fe-bearing phyllosilicates.

Studies of the spectral effects in the mid- to far-infrared wavelength range of mildly heated carbonaceous chondrites have also been limited. One study of experimental heating of the highly altered CM 2.1 ALH 831000 for 24 hours in vacuum at 400°C found no changes to the location of the Si-O bending band minimum with heating (Lindgren et al., 2020). However, upon revisiting the data we find that the Si-O bending band, which is unchanged in position, does decrease in depth with heating (the Si-O stretching band depth remains constant), and is even more strongly shallowed when heated for a longer time period (Fig. 16). We hypothesize that the shallowing of the Si-O bending band reflects the modification and weakening of the Mg-O-Si and/or Fe-O-Si deformation bands as mild heating amorphizes (i.e., breaks crystalline bonds) the Mg- and Fe-bearing phyllosilicate, as has been documented to occur via X-ray diffraction (XRD) and thermogravimetric analysis (TGA) of mildly experimentally and naturally heated carbonaceous chondrites (e.g., Tonui et al., 2014; King et al., 2015; Lindgren et al., 2020;

Matsuoka et al., 2022). Further, multiple studies have demonstrated that Fe-bearing hydrated phases within carbonaceous chondrites decompose at lower temperatures than Mg-bearing phyllosilicates (Caillere and Henin, 1957; King et al., 2015; Mogi et al., 2017; Nakamura et al., 2017; Matsuoka et al., 2022). Therefore, both experimental heating and space weathering studies of CM chondrites support a decreased BBD due to the breakdown of Fe-bearing phyllosilicates.

Simon et al. (2020a) attributed the weak 1.05 µm band on Bennu to Fe-bearing phyllosilicate and/or goethite (iron hydroxide) although its lack of correlation to the 0.55 µm OVIRS band depth (r = -0.17 (0.01)) argues against the latter (Simon et al., 2020a). If it does represent Fe-bearing phyllosilicate, then its correlation to the other spectral parameters (EQ6 BBD, hydration, troilite abundance, albedo) provides further support for the breakdown of Fe-bearing phyllosilicates on Bennu. However, most spectral studies of carbonaceous chondrites place the Fe-bearing phyllosilicate spectral band at 1.1 µm (in contrast to 1.05 µm which is closer to the spectral band position of Fe-bearing olivine) (Hiroi et al., 1996; Cloutis et al., 2012; Matsuoka et al., 2020). Further, several studies document depth reduction of this band upon mild heating (<600°C) (Hiroi et al., 1996; their Fig. 1; Cloutis et al., 2012) and space weathering (Matsuoka et al., 2020). Therefore, it is likely that the 1.05 µm band mapped by OVIRS is an Fe-bearing phyllosilicate band as suggested by Simon et al. (2020a), but may be better characterized by a spectral index centered near 1.1 µm, which the crystal field absorption band for octahedrally-coordinated Fe^{2+} (e.g., Cloutis et al., 2011b). The other spectral band commonly associated of Fe-bearing phyllosilicate in carbonaceous chondrites is the Fe^{3+}/ Fe^{2+} charge transfer band at 0.7 µm (e.g., Cloutis et al., 2011a; Cloutis et al., 2011b; Cloutis et al., 2012), but there was only limited evidence of this band in OVIRS spectra (Simon et al., 2020a) although OCAMS spectral mapping suggested its presence in some low albedo boulders (DellaGiustina et al., 2020). There was no correlation of the EQ6 BBD to the 0.7 µm band map from OCAMS data (r = -0.19 (0.03)). The relative depths of the 0.7 µm and 1.1 µm bands are related to the chemistry of the phyllosilicate, specifically the Fe^{3+}/ Fe^{2+} ratio, as well as the cronstedtite abundance in CMs (Cloutis et al., 2011b), and so this may explain the differences between the 0.7 µm and 1.1 µm band detections on Bennu.

In summary, a shallowing of the EQ6 BBD combined with smaller 1.05 µm band depths, decreased hydration, increased troilite abundance, and lower albedo is most consistent with either space weathering and/or mild (<600°C) heating of phyllosilicates, likely Fe-bearing, within carbonaceous-type material on Bennu.

4.3 Relationships with geomorphology and surface ages

Several studies have pointed out that space weathering of phyllosilicates is analogous to mild heating of these minerals, and therefore results in similar effects (amorphization, dehydroxylation , etc.) (Thompson et al., 2019; Matsuoka et al., 2020; Thompson et al., 2020; Noguchi et al., 2022; Zhang et al., 2022). Specifically, for carbonaceous asteroid Ryugu, it has been argued that dehydration via space weathering is responsible for the weakened 2.7 µm feature on its surface (Noguchi et al., 2022). Therefore, it may be difficult to distinguish which process is responsible for the spectral trends we see on Bennu. If not caused by space weathering, mild heating detected on Bennu's surface could result from solar radiative heating or could have occurred on Bennu's parent body (i.e., from impacts or decay of radiogenic isotopes). Solar radiative heating is similar to space weathering in that it is dependent on the surface exposure age of the material, while mildly heated lithologies derived from Bennu's parent body would be more randomly distributed due to the chaotic disruption and random reaccumulation of fragments that formed the rubble pile (Michel et al., 2020).

In terms of geomorphology, we note that unlike the dust index (EQ3 SR) which is strongly correlated to brecciated, low albedo, low thermal inertia boulders (Fig. 3, 8, 10,12), variation in EQ6 BBD is less correlated to a particular type of terrain. We see a large boulder with a varied EQ6 BBD (in addition to varied 1.05 µm and 2.74 µm band depths and troilite abundance) across it (Fig. 8), as well as some variation in these values between different boulders in the other two areas (Fig. 10, 12). However, consistently in all three areas, the highest EQ6 BBD values (with larger 1.05 µm band depth, higher hydration and albedo, and lower troilite abundance) are always associated with the smallest rocks and unresolved areas (Fig. 8,10,12). If we interpret the EQ6 BBD spectral index as evidence of space weathering or solar radiative heating, this suggests these areas, dominated by small rocks and unresolved areas, are more freshly exposed material on Bennu. Larger, resolvable boulders would have a more varied surface exposure history in this view.

This interpretation is consistent with other studies of Bennu that suggest that smaller rocks and unresolved fines are younger (in regard to total surface exposure) than large boulders. In the Cambioni et al. (2021) model, high porosity boulders would have longer sustained surface exposure than the lower porosity rocks that are more readily broken up by impact to create fresh, overturned regolith. Other studies suggest that mass movement is preferentially moving and removing smaller rocks and grains to bury and/or expose large boulders (several meters in size), implying that areas that do contain smaller rocks are relatively younger (in regards to accumulated surface exposure) than the boulder-rich areas (Jawin et al., 2020; Jawin et al., 2022). In support of this, Ballouz et al. (2020) estimates the exposure history of meter-sized boulders to be 1.75 ± 0.75 Myr, which is much longer than the estimate of mass movement ages on Bennu ($\leq$ 500 kyr; (Jawin et al., 2020; Jawin et al., 2022)). Therefore, if areas dominated by small rocks and unresolved areas on Bennu do have a shorter exposure history, and because these areas are also more highly hydrated with higher EQ6 BBD values, 1.05 µm band depths, albedo, and lower troilite abundance, this argues for either space weathering or solar radiative heating as the cause of the spectral trends we see.

DellaGiustina et al. (2020) identified small ($\leq$ 25 m) craters with the reddest slopes (defined by the OCAMS-derived b′ to x spectral slope) that they interpreted as the most freshly exposed, least space weathered material on Bennu. While individual craters are too small to be detected in the OTES data (40 m spot size), the distribution of these younger, redder craters on the EQ6 BBD map (Fig. 17) does show that in the three local regions examined (Figs. 8, 10, 12), redder craters are identified in the areas where EQ6 BBD, and hydration, is highest. Further, while not a perfect spatial correlation, young, redder craters are mostly absent from the areas of lowest

EQ6 BBD and tend to be located in areas with moderately to high EQ6 BBD. One exception to this trend is the boulder rich area of Figure 10, where some redder craters also overlie the lower EQ6 BBD areas. As discussed above, the relatively small size of the boulders (< 20 m across) with variable spectral signatures, compared to the spot sizes of OTES (~40 m), might be masking the actual variability in EQ6 BBD in this area. Regardless, the general association of the highest EQ6 BBD values (i.e., highest hydration, largest 1.05 µm band depths, and lowest troilite abundance) with the youngest, freshest craters on Bennu further confirms that the dehydration spectral signature evident within the EQ6 BBD is related to surface exposure age, and therefore represents either space weathering or solar radiative heating, and not a heating signature inherited from Bennu's parent body.

4.4 Different space weathering processes on Bennu

Although there is a spatial correlation between high EQ6 BBD values and the reddest (i.e., least space-weathered) craters on Bennu (DellaGiustina et al., 2020), there is not a clear correlation of the EQ6 BBD to other space weathering spectral parameters. MapCam data suggest that space weathering effects in the ultraviolet (UV) to near-infrared (NIR) are evident across Bennu's surface (DellaGiustina et al., 2020). We found no correlation of EQ6 BBD with OCAMS-derived spectral slope maps that may be indicative of space weathering (normalized 0.85/0.55 µm visible slope proxy (r = -0.24 (0.05)) or normalized 0.47/0.55 µm near-UV slope proxy (r = 0.04 (0.02)). Further, we found no correlation of EQ6 BBD with the modeled magnetite abundance maps of (Trang et al., 2021), which are also interpreted to represent a space weathering process. In addition, there is an apparent contradiction in regard to albedo, where small red craters mapped by DellaGiustina et al. (2020) are lower in albedo than their surroundings, implying that Bennu's surface brightens with space weathering. In contrast, we document here a decrease in albedo correlated to decreased hydration, 1.05 µm band depth, BBD values, and increased troilite, implying that Bennu's surface albedo darkens with space weathering (or mild heating). However, Bennu's equatorial bulge, which is interpreted to be the oldest features on Bennu, has a relatively dark albedo, presumably also due to space weathering (Clark et al., 2023).

This apparent contradiction regarding albedo trends on Bennu was attributed by Clark et al. (2023) to different timescales of space weathering processes. They conclude that 'intermediate age' surfaces where the reddest craters are located on Bennu are brighter (and bluer) due to space weathering and thus the fresh red craters are darker compared to their surroundings. They also conclude that the very oldest region on Bennu – the equatorial region – is darkest (and reddest), also due to space weathering, but on a longer time scale. This interpretation is consistent with the relative timescales of different space weathering processes. DellaGiustina et al. (2020) and Jawin et al. (2022) date the reddest craters as produced within the last ~5 x 10^6 years. Timescales of solar wind implantation are estimated to be 10^4-10^6 years (Vernazza et al., 2009; Brunetto et al., 2020), and so it is plausible that these craters were formed in a surface that has evidence of solar wind implantation (in regards to visible albedo and slope). Further, solar wind implantation is the only space weathering process that has shown to increase albedo on carbonaceous chondrites in the lab (Clark et al., 2023).

The timescale for micrometeorite (dust) bombardment to optically modify chondrite surfaces has been estimated to be longer, 10^6- 10^8 years (Sasaki et al., 2001; Matsuoka et al., 2015) and therefore micrometeorite bombardment works to overcome the effects of solar wind implantation (Matsuoka et al., 2015). In addition, micrometeorite bombardment (as well as mild heating; see above) has been shown to consistently lower the albedo of carbonaceous chondrites in the lab (Clark et al., 2023). To summarize, assuming a similar starting composition, freshly exposed surfaces on Bennu first brighten in albedo in response to solar wind implantation, and then darken as micrometeorite bombardment (or solar radiative heating) (Clark et al., 2023) becomes the dominant space weathering (surface alteration) process (Matsuoka et al., 2015).

Our observations of decreased BBD with decreased albedo in addition to decreased 2.74 µm and 1.05 µm band depths and increased troilite abundance likely reflect these longer exposure timescales due to micrometeorite bombardment or alternatively, to mild heating via solar radiation. The fact that the red craters are located primarily in the higher BBD areas support that this material is relatively younger than the lower BBD areas – this is the 'intermediate' age material of Clark et al. (2023), and craters into this material are visibly darker. Again, we hypothesize that the relatively younger age of this higher BBD material is due to more efficient particle overturn in these areas, due to impact into lower porosity material (Cambioni et al., 2022) or mass wasting processes (Jawin et al. 2020; 2022).

The lowest BBD values could therefore record the longest-term surface exposure of materials on Bennu. While the equatorial bulge (mapped from (Jawin et al., 2022)) is not uniformly lowest in BBD, the distribution of lowest BBD values is highly spatially consistent with the lowest OLA-derived normal albedo at 1064 nm (Clark et al., 2023), especially within and near the equatorial bulge (Fig. 17). Clark et al. (2023) interpreted the darkest OLA-derived normal albedo values in the equatorial region to be indicative of longer exposure to space weathering, and our data supports that interpretation. As discussed previously, most of these oldest exposed surfaces are boulder faces or boulder-rich regions (Figs. 8,10, 12), which is consistent with the relatively old cratering age derived for exposed boulders (1.75 ± 0.75 Myr; (Ballouz et al., 2020)). However, not all boulders have the lowest BBD values (Figs. 10, 12). This could be due to either lithologic (compositional) variation among different boulder types that result in different responses to space weathering (DellaGiustina et al., 2020; Clark et al., 2023), the varied exposure history of individual boulders related to burial, excavation, or mass movement (Jawin et al. 2020; 2022), or a combination of these two scenarios.

Finally, we note that some of the oldest exposures of material on Bennu as revealed by the EQ6 BBD fall within the Rugged Unit of Jawin et al. (2022), which they interpreted to have been resurfaced within the past 500,000 years (Fig. 17). However, these areas could have still experienced mass movement while retaining the relatively old exposure histories of larger rocks and boulders. For example, Roc Saxum is mapped as part of this younger Rugged Unit (Jawin et al., 2022) but Jawin et al. (2020) mapped the movement of small rocks northward across Roc Saxum (see their Fig. 1a), resulting in its partial burial proceeding from the south.

And there is increased hydration, EQ6 BBD values, 1.05 µm band depths, and albedo, and lower troilite abundance on the southern edge of the boulder (Fig. 8), consistent with this interpretation of fresher material burying a relatively older (longer surface exposure) boulder. Therefore, although there may not be clear and widespread mass movement indicators in the Smooth Unit, which Jawin et al. (2022) interpreted as not being significantly resurfaced in the past 2 million years, smaller particles and rocks in this unit may still be experiencing some movement and overturn, exposing relatively fresher material with correspondingly larger BBD, increased hydration, larger 1.05 µm band depth, higher albedo, and lower troilite abundance.

4.5 Micrometeorite bombardment or solar radiative heating?

As discussed above, the long exposure ages and lower albedo of the lowest BBD areas are more consistent with micrometeorite bombardment compared to solar wind implantation (Clark et al., 2023). Therefore, if variation in EQ6 BBD is caused by space weathering, we favor micrometeorite bombardment as the primary process responsible for the correlated spectral changes that we document here. However, these spectral observations are also consistent with mild heating of carbonaceous chondrites, and the relation of the BBD to surface exposure age suggests solar radiative heating as a possible cause.

The exact temperature at which dehydroxylation and dehydration occur within phyllosilicate depends on chemistry, physical structure (bulk or particulate), and timescale of heating, but most studies converge on a lower threshold of about 300 °C (573 K), with the breakdown of Fe-bearing phyllosilicate occurring at lower temperature (e.g., Caillere and Henin, 1957; Nakamura, 2005; Lindgren et al., 2020; King et al., 2021; Velbel and Zolensky, 2021; Matsuoka et al., 2022). However, recent experimental heating of CM Murchison showed that spectral changes occur after heating to 200 °C for 111 days, including darkening and a loss of the 0.7 µm band, which could indicate modification of Fe-bearing phyllosilicate (Sidhu et al., 2023). Therefore, perhaps sustained temperatures below 300 °C could result in dehydroxylation/dehydration of Fe-bearing phyllosilicates.

The current maximum temperature of Bennu's surface is ~97 °C (370K) (Rozitis et al., 2020) and therefore seems insufficient to cause phyllosilicate dehydroxylation. And while there is evidence for thermally-induced exfoliation, cracking, and fracturing of boulders on Bennu, this is driven by mechanical stresses due to diurnal temperature changes that are occurring at or below the current surface temperatures on Bennu (Molaro et al., 2020a; Molaro et al., 2020b; Delbo et al., 2022). However, as noted by previous studies, there does seem to be a temperature correlation to the hydration state of Bennu's surface (Simon et al., 2020a; Simon et al., 2020b). These studies also documented a strong correlation of surface temperature to albedo and 1.05 µm band depth (both r = -0.65) (Simon et al., 2020a; Simon et al., 2020b). Similarly, we find a correlation of EQ6 BBD (r = -0.53 (0.08)) to EQ3 (12:30 pm LST) surface temperature (Rozitis et al., 2020), but modeled nanophase troilite abundance of Trang et al. (2021) is uncorrelated to temperature (r = 0.38 (0.14)). If the current surface temperatures are too low to dehydroxylate phyllosilicates, is this a record of higher temperatures in the past?

Based on dynamical and thermal modeling Delbo and Michel (2011) calculated a <25% probability that 50% of Bennu's surface was heated to ≥ 573 K (300 °C) and a ~50% probability that it was heated to 500 K (227 °C). The cumulative time that the surface was exposed to each of these temperatures based on their model was ~0.75 Myr and ~1 Myr, respectively, which is consistent with the latest estimate of Bennu's lifetime in near Earth space 1.75 ± 0.75 Myr (Ballouz et al., 2020).

There are other OSIRIS-REx results that indicate heating could have modified Bennu's surface materials. First, a study of the OVIRS-derived H content for Bennu's surface found it to be most consistent with naturally heated CMs (and C2 Tagish Lake) (Praet et al., 2021). Second, there is lack of a detectable Mg-OH band near 15.5 µm (625 cm^{-1}) in all Bennu OTES EQ3 and EQ6 spectra. This band is a prominent spectral feature in all CM chondrite TIR spectra (Hanna et al., 2020) and has been shown to weaken and eventually disappear with heating (Fig. 19) (Hanna et al., 2020; Lindgren et al., 2020). The 15.5 µm Mg-OH band has been detected in particulates covering the OTES optics after the TAG sampling event (Lauretta et al., 2022), and could represent material, perhaps excavated from depth, that experienced less heating (or less space weathering (Lauretta et al., 2022; Praet et al., 2022)). However, it could also represent material with a different phyllosilicate chemistry than the material that dominates Bennu's surface, as it appears to have a different CF location, Si-O stretching band minimum and shape, and low wavenumber emissivity maximum ((Lauretta et al., 2022) their Fig. 6). Hamilton et al. (2022) also noted the different Si-O stretching band shape, suggesting that a CR1 (GRO 95577) may be a better spectral match to Bennu. Therefore, the particulates on the OTES optics, and by extension perhaps also the returned sample, may represent either a less heated or space weathered material, or a material with a different composition, than that of other Bennu surfaces.

In summary, our global and local analyses suggest that the OTES EQ6 BBD spectral index is an indicator of modification of phyllosilicate, likely Fe-bearing, caused by either space weathering (likely micrometeorite bombardment) or mild heating from solar radiation on Bennu's surface. It appears to be an indicator of surface exposure age of material on Bennu, whereby the lowest BBD values reflect the longest-term exposure, and the highest BBD values are associated with material that has been more recently exposed due to movement or overturn from impact or mass wasting processes. The BBDis correlated to OVIRS indices that indicate hydration level (2.74 µm band depth, NOPL, ESPAT (Kaplan et al., 2020a; Praet et al., 2021)), Fe-phyllosilicate abundance (1.05 µm band depth (Simon et al., 2020a)), nanophase troilite abundance (Trang et al., 2021), and albedo (Li et al., 2021) on both global and localized scales, although the global correlation of these indices is not strong in all cases likely due to: 1) the difference in spot size between the OTES (~ 40 m) and OVIRS (~20 m) instruments and 2) spatial variation in degree of heating/space weathering that is below the size of the OTES spot size. Finally, we note that this mild heating or space weathering process is also likely modifying the silicate stretching region as laboratory studies suggest (Brunetto et al., 2020; Lindgren et al., 2020) and requires future investigation.

4.6 Predictions for the returned sample

The TAG sampling site is located in an area of moderate EQ6 BBD values within a young, red crater named Hokioi (Fig. 17) and OCAMS data indicate the sampling site surface is relatively less space weathered and more freshly exposed compared to the rest of Bennu's surface, even before sampling (DellaGiustina et al., 2020; Lauretta et al., 2022). This, in addition to the fact that TAGSAM likely collected material below the surface, suggests most of the returned material may show minimal signs of space weathering or solar radiative heating. For any grains that may be space weathered or mildly heated we would expect, based on our results, that these would be characterized by a decreased 2.7 µm band depth, a decreased 1.05 (or 1.10) µm band depth, a decreased Si-O bending band (22.7 µm) depth, and increased sulfide (possibly troilite) abundance. These grains would also likely have chemical and textural evidence of dehydration/dehydroxylation including a lower H content and amorphous or poorly crystalline phyllosilicates. All of these space weathering indicators may be limited to the outer layer of the grain, similar to what has been seen for space weathered Ryugu grains (Noguchi et al., 2022) and experimentally irradiated carbonaceous grains (Matsuoka et al., 2015; Matsuoka et al., 2020; Laczniak et al., 2021). We further hypothesize that solar radiative heating may not cause the vesiculated textures and splash melt products typically associated with space weathered grains (Matsuoka et al., 2015; Matsuoka et al., 2020; Laczniak et al., 2021) as these have not been reported in mildly heated carbonaceous chondrites. Therefore, analysis of these grains in the returned sample will hopefully inform on the process responsible for phyllosilicate modification on Bennu's surface.

Acknowledgements

We are grateful to the entire OSIRIS-REx Team for making the encounter with Bennu possible. This material is based upon work supported by NASA under Contract NNM10AA11C issued through the New Frontiers Program. R.D.H. was supported by the OSIRIS-REx Participating Scientist Program – Grant 80NSSC18K0229. We thank Rosario Brunetto for sharing laboratory spectra, and David Trang, Alice Praet, and Daniella DellaGiustina for sharing spectral maps from their work. We are grateful to Andrew Ryan and Ben Rozitis for sharing data and code for data processing and for useful discussions regarding temperature trends on Bennu. We thank Martin Lee for his help in the experiemental heating of ALH 83100 and Erica Jawin for enlightening discussions regarding mass movment and boulder exposure on Bennu.

Data Availability

OSIRIS-REx data are available via the Planetary Data System at https://sbn.psi.edu/pds/resource/orex/.

References

Ballouz R. L., Walsh K. J., Barnouin O. S., DellaGiustina D. N., Asad M. A., Jawin E. R., Daly M. G., Bottke W. F., Michel P., Avdellidou C., Delbo M., Daly R. T., Asphaug E., Bennett C. A., Bierhaus E. B., Connolly H. C., Golish D. R., Molaro J. L., Nolan M. C., Pajola M., Rizk B., Schwartz S. R., Trang D., Wolner C. W. V. and Lauretta D. S. (2020) Bennu's near-Earth lifetime of 1.75 million years inferred from craters on its boulders. *Nature* **587**, 205-209.

Barnouin O. S., Daly M. G., Palmer E. E., Gaskell R. W., Weirich J. R., Johnson C. L., Asad M. M. A., Roberts J. H., Perry M. E., Susorney H. C. M., Daly R. T., Bierhaus E. B., Seabrook J. A., Espiritu R. C., Nair A. H., Nguyen L., Neumann G. A., Ernst C. M., Boynton W. V., Nolan M. C., Adam C. D., Moreau M. C., Risk B., D'Aubigny C. D., Jawin E. R., Walsh K. J., Michel P., Schwartz S. R., Ballouz R. L., Mazarico E. M., Scheeres D. J., McMahon J., Bottke W., Sugita S., Hirata N., Hirata N., Watanabe S., Burke K. N., DellaGuistina D. N., Bennett C. A. and Lauretta D. S. (2019) Shape of (101955) Bennu indicative of a rubble pile with internal stiffness. *Nat Geosci* **12**, 247-252.

Bennett C. A., DellaGiustina D. N., Becker K. J., Becker T. L., Edmundson K. L., Golish D. R., Bennett R. J., Burke K. N., Cue C. N. U., Clark B. E., Contreras J., Deshapriya J. D. P., d'Aubigny C. D., Fitzgibbon G., Jawin E. R., Nolan T. Q., Porter N. A., Riehl M. M., Roper H. L., Rizk B., Tang Y., Zeszut Z., Gaskell R. W., Palmer E. E., Weirich J. R., Al Asad M. M., Philpott L., Daly M. G., Barnouin O. S., Enos H. L. and Lauretta D. S. (2021) A high-resolution global basemap of (101955) Bennu. *Icarus* **357**, 113690.

Breitenfeld L. B., Rogers A. D., Glotch T. D., Kaplan H. H., Hamilton V. E. and Christensen P. R. (2022) Mapping Phyllosilicates on the Asteroid Bennu Using Thermal Emission Spectra and Machine Learning Model Applications. *Geophysical Research Letters* **49**, e2022GL100815.

Brunetto R., Lantz C., Nakamura T., Baklouti D., Le Pivert-Jolivet T., Kobayashi S. and Borondics F. (2020) Characterizing irradiated surfaces using IR spectroscopy. *Icarus* **345**, 113722.

Caillere S. and Henin S. (1957) The chlorite and serpentine minerals. In *The Differential Thermal Investigations of Clays* (ed. R.C. Mackenzie). Mineralogical Society, London. pp. 207-230.

Cambioni S., Delbo M., Poggiali G., Avdellidou C., Ryan A. J., Deshapriya J. D. P., Asphaug E., Ballouz R. L., Barucci M. A., Bennett C. A., Bottke W. F., Brucato J. R., Burke K. N., Cloutis E., DellaGiustina D. N., Emery J. P., Rozitis B., Walsh K. J. and Lauretta D. S. (2021) Fine-regolith production on asteroids controlled by rock porosity. *Nature* **598**, 49-52.

Christensen P., Hamilton V., Anwar S., Mehall G. and Lauretta D. (2019a). *Origins, Spectral Interpretation, Resource Identification, Security, Regolith Explorer (OSIRIS-REx): OSIRIS-REx Thermal Emission Spectrometer Bundle, urn:nasa:pds:orex.otes*, NASA Planetary Data System.

Christensen P., Hamilton V., Anwar S., Mehall G. and Lauretta D. S. (2019b) Origins, Spectral Interpretation, Resource Identification, Security, Regolith Explorer (OSIRIS-REx): OSIRIS-REx Thermal Emission Spectrometer Document Collection. *NASA Planetary Data System*.

Christensen P. R., Anwar S., Burris M. E., Carter S. R., Dickenshied S., Noss D. D., Hagee W. R., Rios K. J. and Wren P. F. (2018a). *J-Asteroid: JMARS for Asteroids and Other Small Bodies*, Lunar and Planetary Science Conference XLIX, The Woodlands, TX, p. 2788.

Christensen P. R., Engle E., Anwar S., Dickenshied S., Noss D., Gorelick N. and Weiss-Malik M. (2009) JMARS - A Planetary GIS. *American Geophysical Union Fall Meeting.* San Francisco.

Christensen P. R., Hamilton V. E., Mehall G. L., Pelham D., O'Donnell W., Anwar S., Bowles H., Chase S., Fahlgren J., Farkas Z., Fisher T., James O., Kubik I., Lazbin I., Miner M., Rassas M., Schulze L., Shamordola K., Tourville T., West G., Woodward R. and Lauretta D. (2018b) The OSIRIS-REx Thermal Emission Spectrometer (OTES) Instrument. *Space Science Reviews* **214**, 87.

Clark B. E., Sen A., Zou X. D., DellaGiustina D. N., Sugita S., Sakatani N., Thompson M., Trang D., Tatsumi E., Barucci M. A., Barker M., Campins H., Morota T., Lantz C., Hendrix A. R., Vilas F., Keller L., Hamilton V. E., Kitazato K., Sasaki S., Matsuoka M., Nakamura T., Praet A., Ferrone S. M., Hiroi T., Kaplan H. H., Bottke W. F., Li J. Y., Le Corre L., Molaro J. L., Ballouz R. L., Hergenrother C. W., Rizk B., Burke K. N., Bennett C. A., Golish D. R., Howell E. S., Becker K., Ryan A. J., Emery J. P., Fornasier S., Simon A. A., Reuter D. C., Lim L. F., Poggiali G., Michel P., Delbo M., Barnouin O. S., Jawin E. R., Pajola M., Riu L., Okada T., Deshapriya J. D. P., Brucato J. R., Binzel R. P. and Lauretta D. S. (2023) Overview of the search for signs of space weathering on the low-albedo asteroid (101955) Bennu. *Icarus* **400**, 115563.

Cloutis E. A., Hiroi T., Gaffey M. J., Alexander C. M. O. D. and Mann P. (2011a) Spectral reflectance properties of carbonaceous chondrites: 1. CI chondrites. *Icarus* **212**, 180-209.

Cloutis E. A., Hudon P., Hiroi T. and Gaffey M. J. (2012) Spectral reflectance properties of carbonaceous chondrites 4: Aqueously altered and thermally metamorphosed meteorites. *Icarus* **220**, 586-617.

Cloutis E. A., Hudon P., Hiroi T., Gaffey M. J. and Mann P. (2011b) Spectral reflectance properties of carbonaceous chondrites: 2. CM chondrites. *Icarus* **216**, 309-346.

Curran P. A. (2014) Monte Carlo error analyses of Spearman's rank test. *arXiv e-prints*, arXiv:1411.3816.

Delbo M. and Michel P. (2011) Temperature history and dynamical evolution of (101955) 1999 RQ 36: A potential target for sample return from a primitive asteroid. *The Astrophysical Journal Letters* **728**, L42.

Delbo M., Walsh K. J., Matonti C., Wilkerson J., Pajola M., Al Asad M. M., Avdellidou C., Ballouz R.-L., Bennett C. A., Connolly H. C., DellaGiustina D. N., Golish D. R., Molaro J. L., Rizk B., Schwartz S. R. and Lauretta D. S. (2022) Alignment of fractures on Bennu's boulders indicative of rapid asteroid surface evolution. *Nature Geoscience* **15**, 453-457.

DellaGiustina D. N., Burke K. N., Walsh K. J., Smith P. H., Golish D. R., Bierhaus E. B., Ballouz R. L., Becker T. L., Campins H., Tatsumi E., Yumoto K., Sugita S., Deshapriya J. D. P., Cloutis E. A., Clark B. E., Hendrix A. R., Sen A., Al Asad M. M., Daly M. G., Applin D. M., Avdellidou C., Barucci M. A., Becker K. J., Bennett C. A., Bottke W. F., Brodbeck J. I., Connolly H. C., Delbo M., de Leon J., Drouet d'Aubigny C. Y., Edmundson K. L., Fornasier S., Hamilton V. E., Hasselmann P. H., Hergenrother C. W., Howell E. S., Jawin E. R., Kaplan H. H., Le Corre L., Lim L. F., Li J. Y., Michel P., Molaro J. L., Nolan M. C., Nolau J., Pajola M., Parkinson A., Popescu M., Porter N. A., Rizk B., Rizos J. L., Ryan A. J., Rozitis B., Shultz N. K., Simon A. A., Trang D., Van Auken R. B., Wolner C. W. V. and Lauretta D. S. (2020) Variations in color and reflectance on the surface of asteroid (101955) Bennu. *Science* **370**, eabc3660.

Ferrone S. M., Clark B. E., Hawley C. L., Joseph J., Nolan M. C., Bennett C., Zou X.-D., Selznick S., Loveridge M., Deshapriya P. and Lauretta D. S. (2021) Analysis of Projection Effects in OSIRIS-REx Spectral Mapping Methods: Recommended Protocols for Facet-Based Mapping. *Earth and Space Science* **8**, e2020EA000613.

Garenne A., Beck P., Montes-Hernandez G., Chiriac R., Toche F., Quirico E., Bonal L. and Schmitt B. (2014) The abundance and stability of “water” in type 1 and 2 carbonaceous chondrites (CI, CM and CR). *Geochim. Cosmoch. Acta* **137**, 93-112.

Graff T. G. (2003). *Effects of dust coatings on visible, near-infrared, thermal emission, and Mossbauer spectra: Implications for mineralogical remote sensing of Mars*, Geology. Arizona State University, Temp, p. 106.

Hamilton V. E., Christensen P. R., Kaplan H., Haberle C., Rogers A. D., Glotch T., Breitenfeld L., Goodrich C. A., Schrader D. L., McCoy T., Lantz C., Hanna R. D., Simon A. A., Brucato J. R., Clark B. and Lauretta D. (2021) Evidence for limited compositional and particle size variation on asteroid (101955) Bennu from thermal infrared spectroscopy. *Astronomy and Astro-Physics* **650**, 13.

Hamilton V. E., Kaplan H. H., Connolly H. C., Goodrich C. A., Abreu N. M. and Simon A. A. (2022) GRO 95577 (CR1) as a mineralogical analogue for asteroid (101955) Bennu. *Icarus* **383**, 115054.

Hamilton V. E., Simon A. A., Christensen P. R., Reuter D. C., Clark B. E., Barucci M. A., Bowles N. E., Boynton W. V., Brucato J. R., Cloutis E. A., Connolly H. C., Donaldson Hanna K. L., Emery J. P., Enos H. L., Fornasier S., Haberle C. W., Hanna R. D., Howell E. S., Kaplan H. H., Keller L. P., Lantz C., Li J. Y., Lim L. F., McCoy T. J., Merlin F., Nolan M. C., Praet A., Rozitis B., Sandford S. A., Schrader D. L., Thomas C. A., Zou X. D., Lauretta D. S. and Team’ t. O.-R. (2019) Evidence for widespread hydrated minerals on asteroid (101955) Bennu. *Nature Astronomy* **3**, 332-340.

Hanna R. D., Hamilton V. E., Haberle C. W., King A. J., Abreu N. M. and Friedrich J. M. (2020) Distinguishing relative aqueous alteration and heating among CM chondrites with IR spectroscopy. *Icarus* **346**, 113760.

Hergenrother C. W., Maleszewski C., Li J. Y., Pajola M., Chesley S. R., French A. S., Davis A. B., Pelgrift J. Y., Leonard J. M., Shelly F., Liounis A. J., Becker K., Balram-Knutson S. S., Garcia R., Kareta T. R., Adam C., Alkiek K., Bos B. J., Brozović M., Burke K. N., Christensen E., Clark B. E., DellaGiustina D. N., Drouet d'Aubigny C., Farnocchia D., Howell E. S., Jacobson R. A., Kidd J. N., Lessac-Chenen E. J., Melikyan R., Nolan M. C., Park R. S., Selznick S., Rizk B. and Lauretta D. S.

(2020) Photometry of Particles Ejected From Active Asteroid (101955) Bennu. *Journal of Geophysical Research: Planets* **125**, e2020JE006381.

Hiroi T., Zolensky M. E., Pieters C. M. and Lipschutz M. E. (1996) Thermal metamorphism of the C, G, B, and F asteroids seen from the 0.7 µm, 3 µm, and UV absorption strengths in comparison with carbonaceous chondrites. *Meteoritics & Planetary Science* **31**, 321-327.

Jawin E. R., McCoy T. J., Walsh K. J., Connolly H. C., Ballouz R. L., Ryan A. J., Kaplan H. H., Pajola M., Hamilton V. E., Barnouin O. S., Emery J. P., Rozitis B., DellaGiustina D. N., Daly M. G., Bennett C. A., Golish D. R., Perry M. E., Daly R. T., Bierhaus E. B., Nolan M. C., Enos H. L. and Lauretta D. S. (2022) Global geologic map of asteroid (101955) Bennu indicates heterogeneous resurfacing in the past 500,000 years. *Icarus* **381**, 114992.

Jawin E. R., Walsh K. J., Barnouin O. S., McCoy T. J., Ballouz R. L., DellaGiustina D. N., Connolly Jr H. C., Marshall J., Beddingfield C., Nolan M. C., Molaro J. L., Bennett C. A., Scheeres D. J., Daly M. G., Al Asad M., Daly R. T., Bierhaus E. B., Susorney H. C. M., Kaplan H. H., Enos H. L. and Lauretta D. S. (2020) Global Patterns of Recent Mass Movement on Asteroid (101955) Bennu. *Journal of Geophysical Research: Planets* **125**, e2020JE006475.

Kaplan H. H., Hamilton V. E., Howell E. S., Scott Anderson F., Barrucci M. A., Brucato J., Burbine T. H., Clark B. E., Cloutis E. A., Connolly Jr H. C., Dotto E., Emery J. P., Fornasier S., Lantz C., Lim L. F., Merlin F., Praet A., Reuter D. C., Sandford S. A., Simon A. A., Takir D. and Lauretta D. S. (2020a) Visible–near infrared spectral indices for mapping mineralogy and chemistry with OSIRIS-REx. *Meteoritics & Planetary Science* **55**, 744-765.

Kaplan H. H., Lauretta D. S., Simon A. A., Hamilton V. E., DellaGiustina D. N., Golish D. R., Reuter D. C., Bennett C. A., Burke K. N., Campins H., Connolly H. C., Dworkin J. P., Emery J. P., Glavin D. P., Glotch T. D., Hanna R., Ishimaru K., Jawin E. R., McCoy T. J., Porter N., Sandford S. A., Ferrone S., Clark B. E., Li J. Y., Zou X. D., Daly M. G., Barnouin O. S., Seabrook J. A. and Enos H. L. (2020b) Bright carbonate veins on asteroid (101955) Bennu: Implications for aqueous alteration history. *Science*, eabc3557.

King A. J., Schofield P. F. and Russell S. S. (2021) Thermal alteration of CM carbonaceous chondrites: Mineralogical changes and metamorphic temperatures. *Geochim. Cosmoch. Acta* **298**, 167-190.

King A. J., Solomon J. R., Schofield P. F. and Russell S. S. (2015) Characterising the CI and CI-like carbonaceous chondrites using thermogravimetric analysis and infrared spectroscopy. *Earth, Planets and Space* **67**, 198.

Laczniak D. L., Thompson M. S., Christoffersen R., Dukes C. A., Clemett S. J., Morris R. V. and Keller L. P. (2021) Characterizing the spectral, microstructural, and chemical effects of solar wind irradiation on the Murchison carbonaceous chondrite through coordinated analyses. *Icarus* **364**, 114479.

Lantz C., Hamilton V. E., Hanna R. D., Brunetto R., Christensen P. R. and Lauretta D. (2020) Can we detect space weathering on bennu using otes data? *Lunar and Planetary Science Conference LI.* Houston, TX. #1850(abstr.).

Lauretta D. S., Adam C. D., Allen A. J., Ballouz R.-L., Barnouin O. S., Becker K. J., Becker T., Bennett C. A., Bierhaus E. B., Bos B. J., Burns R. D., Campins H., Cho Y., Christensen P. R., Church E. C. A., Clark B. E., Connolly H. C., Daly M. G., DellaGiustina D. N., Drouet d'Aubigny C. Y., Emery J. P., Enos H. L., Kasper S. F., Garvin J. B., Getzandanner K., Golish D. R., Hamilton V. E., Hergenrother C. W., Kaplan H. H., Keller L. P., Lessac-Chenen E. J., Liounis A. J., Ma H., McCarthy L. K., Miller B. D., Moreau M. C., Morota T., Nelson D. S., Nolau J. O., Olds R., Pajola M., Pelgrift J. Y., Polit A. T., Ravine M. A., Reuter D. C., Rizk B., Rozitis B., Ryan A. J., Sahr E. M., Sakatani N., Seabrook J. A., Selznick S. H., Skeen M. A., Simon A. A., Sugita S., Walsh K. J., Westermann M. M., Wolner C. W. V. and Yumoto K. (2022) Spacecraft sample collection and subsurface excavation of asteroid (101955) Bennu. *Science* **377**, 285-291.

Lauretta D. S., DellaGiustina D. N., Bennett C. A., Golish D. R., Becker K. J., Balram-Knutson S. S., Barnouin O. S., Becker T. L., Bottke W. F., Boynton W. V., Campins H., Clark B. E., Connolly H. C., Drouet d'Aubigny C. Y., Dworkin J. P., Emery J. P., Enos H. L., Hamilton V. E., Hergenrother C. W., Howell E. S., Izawa M. R. M., Kaplan H. H., Nolan M. C., Rizk B., Roper H. L., Scheeres D. J., Smith P. H., Walsh K. J., Wolner C. W. V., Highsmith D. E., Small J., Vokrouhlický D., Bowles N. E., Brown E., Donaldson Hanna K. L., Warren T., Brunet C., Chicoine R. A., Desjardins S., Gaudreau D., Haltigin T., Millington-Veloza S., Rubi A., Aponte J., Gorius N., Lunsford A., Allen B., Grindlay J., Guevel D., Hoak D., Hong J., Schrader D. L., Bayron J., Golubov O., Sánchez P., Stromberg J., Hirabayashi M., Hartzell C. M., Oliver S., Rascon M., Harch A., Joseph J., Squyres S., Richardson D., Emery J. P., McGraw L., Ghent R., Binzel R. P., Asad M. M. A., Johnson C. L., Philpott L., Susorney H. C. M., Cloutis E. A., Hanna R. D., Connolly H. C., Ciceri F., Hildebrand A. R., Ibrahim E. M., Breitenfeld L., Glotch T., Rogers A. D., Clark B. E., Ferrone S., Thomas C. A., Campins H., Fernandez Y., Chang W., Cheuvront A., Trang D., Tachibana S., Yurimoto H., Brucato J. R., Poggiali G., Pajola M., Dotto E., Epifani E. M., Crombie M. K., Lantz C., Izawa M. R. M., de Leon J., Licandro J., Garcia J. L. R., Clemett S., Thomas-Keprta K., Van wal S., Yoshikawa M., Bellerose J., Bhaskaran S., Boyles C., Chesley S. R., Elder C. M., Farnocchia D., Harbison A., Kennedy B., Knight A., Martinez-Vlasoff N., Mastrodemos N., McElrath T., Owen W., Park R., Rush B., Swanson L., Takahashi Y., Velez D., Yetter K., Thayer C., Adam C., Antreasian P., Bauman J., Bryan C., Carcich B., Corvin M., Geeraert J., Hoffman J., Leonard J. M., Lessac-Chenen E., Levine A., McAdams J., McCarthy L., Nelson D., Page B., Pelgrift J., Sahr E., Stakkestad K., Stanbridge D., Wibben D., Williams B., Williams K., Wolff P., Hayne P., Kubitschek D., Barucci M. A., Deshapriya J. D. P., Fornasier S., Fulchignoni M., Hasselmann P., Merlin F., Praet A., Bierhaus E. B., Billett O., Boggs A., Buck B., Carlson-Kelly S., Cerna J., Chaffin K., Church E., Coltrin M., Daly J., Deguzman A., Dubisher R., Eckart D., Ellis D., Falkenstern P., Fisher A., Fisher M. E., Fleming P., Fortney K., Francis S., Freund S., Gonzales S., Haas P., Hasten A., Hauf D., Hilbert A., Howell D., Jaen F., Jayakody N., Jenkins M., Johnson K., Lefevre M., Ma H., Mario C., Martin K., May C., McGee M., Miller B., Miller C., Miller G., Mirfakhrai A., Muhle E., Norman C., Olds R., Parish C., Ryle M., Schmitzer M., Sherman P., Skeen M., Susak M., Sutter B., Tran Q., Welch C., Witherspoon R., Wood J., Zareski J., Arvizu-Jakubicki M., Asphaug E., Audi E., Ballouz R. L., Bandrowski R., Becker

K. J., Becker T. L., Bendall S., Bennett C. A., Bloomenthal H., Blum D., Boynton W. V., Brodbeck J., Burke K. N., Chojnacki M., Colpo A., Contreras J., Cutts J., Drouet d'Aubigny C. Y., Dean D., DellaGiustina D. N., Diallo B., Drinnon D., Drozd K., Enos H. L., Enos R., Fellows C., Ferro T., Fisher M. R., Fitzgibbon G., Fitzgibbon M., Forelli J., Forrester T., Galinsky I., Garcia R., Gardner A., Golish D. R., Habib N., Hamara D., Hammond D., Hanley K., Harshman K., Hergenrother C. W., Herzog K., Hill D., Hoekenga C., Hooven S., Howell E. S., Huettner E., Janakus A., Jones J., Kareta T. R., Kidd J., Kingsbury K., Balram-Knutson S. S., Koelbel L., Kreiner J., Lambert D., Lauretta D. S., Lewin C., Lovelace B., Loveridge M., Lujan M., Maleszewski C. K., Malhotra R., Marchese K., McDonough E., Mogk N., Morrison V., Morton E., Munoz R., Nelson J., Nolan M. C., Padilla J., Pennington R., Polit A., Ramos N., Reddy V., Riehl M., Rizk B., Roper H. L., Salazar S., Schwartz S. R., Selznick S., Shultz N. and The O.-R. T. (2019a) The unexpected surface of asteroid (101955) Bennu. *Nature* **568**, 55-60.

Lauretta D. S., Enos H. L., Polit A. T., Roper H. L. and Wolner C. W. V. (2021) Chapter 8 - OSIRIS-REx at Bennu: Overcoming challenges to collect a sample of the early Solar System. In *Sample Return Missions* (ed. A. Longobardo). Elsevier. pp. 163-194.

Lauretta D. S., Hergenrother C. W., Chesley S. R., Leonard J. M., Pelgrift J. Y., Adam C. D., Al Asad M., Antreasian P. G., Ballouz R.-L., Becker K. J., Bennett C. A., Bos B. J., Bottke W. F., Brozović M., Campins H., Connolly H. C., Daly M. G., Davis A. B., de León J., DellaGiustina D. N., Drouet d'Aubigny C. Y., Dworkin J. P., Emery J. P., Farnocchia D., Glavin D. P., Golish D. R., Hartzell C. M., Jacobson R. A., Jawin E. R., Jenniskens P., Kidd J. N., Lessac-Chenen E. J., Li J.-Y., Libourel G., Licandro J., Liounis A. J., Maleszewski C. K., Manzoni C., May B., McCarthy L. K., McMahon J. W., Michel P., Molaro J. L., Moreau M. C., Nelson D. S., Owen W. M., Rizk B., Roper H. L., Rozitis B., Sahr E. M., Scheeres D. J., Seabrook J. A., Selznick S. H., Takahashi Y., Thuillet F., Tricarico P., Vokrouhlický D. and Wolner C. W. V. (2019b) Episodes of particle ejection from the surface of the active asteroid (101955) Bennu. **366**, eaay3544.

Li J.-Y., Zou X.-D., Golish D. R., Clark B. E., Ferrone S., Fornasier S., Hasselmann P. H., Ryan A. J., Rozitis B., Emery J. P., Siegler M. A., Simon A. A., DellaGiustina D. N., Reuter D. C., Hamilton V. E. and Lauretta D. S. (2021) Spectrophotometric Modeling and Mapping of (101955) Bennu. *The Planetary Science Journal* **2**, 117.

Lindgren P., Lee M. R., Sparkes R., Greenwood R. C., Hanna R. D., Franchi I. A., King A. J., Floyd C., Martin P.-E., Hamilton V. E. and Haberle C. (2020) Signatures of the post-hydration heating of highly aqueously altered CM carbonaceous chondrites and implications for interpreting asteroid sample returns. *Geochim. Cosmoch. Acta* **289**, 69-92.

Matsuoka M., Nakamura T., Hiroi T., Okumura S. and Sasaki S. (2020) Space Weathering Simulation with Low-energy Laser Irradiation of Murchison CM Chondrite for Reproducing Micrometeoroid Bombardments on C-type Asteroids. *The Astrophysical Journal Letters* **890**, L23.

Matsuoka M., Nakamura T., Kimura Y., Hiroi T., Nakamura R., Okumura S. and Sasaki S. (2015) Pulse-laser irradiation experiments of Murchison CM2 chondrite for reproducing space weathering on C-type asteroids. *Icarus* **254**, 135-143.

Matsuoka M., Nakamura T., Miyajima N., Hiroi T., Imae N. and Yamaguchi A. (2022) Spectral and mineralogical alteration process of naturally-heated CM and CY chondrites. *Geochim. Cosmoch. Acta* **316**, 150-167.

Merlin F., Deshapriya J. D. P., Fornasier S., Barucci M. A., Praet A., Hasselmann P. H., Clark B. E., Hamilton V. E., Simon A. A., Reuter D. C., Zou X.-D., Li J.-Y., Schrader D. L. and Lauretta D. S. (2021) In search of Bennu analogs: Hapke modeling of meteorite mixtures. *A&A* **648**, A88.

Michel P., Ballouz R. L., Barnouin O. S., Jutzi M., Walsh K. J., May B. H., Manzoni C., Richardson D. C., Schwartz S. R., Sugita S., Watanabe S., Miyamoto H., Hirabayashi M., Bottke W. F., Connolly H. C., Yoshikawa M. and Lauretta D. S. (2020) Collisional formation of top-shaped asteroids and implications for the origins of Ryugu and Bennu. *Nature Communications* **11**, 2655.

Milliken R. E. and Mustard J. F. (2007) Estimating the water content of hydrated minerals using reflectance spectroscopy: II. Effects of particle size. *Icarus* **189**, 574-588.

Mogi K., Yamashita S., Nakamura T., Matsuoka M., Okumura S. and Furukawa Y. (2017) Dehydration Process of Experimentally Heated Murchison Without any Effects of Adsorbed and Rehydrated Water. *80th Annual Meeting of the Meteoritical Society.* #6225(abstr.).

Molaro J. L., Hergenrother C. W., Chesley S. R., Walsh K. J., Hanna R. D., Haberle C. W., Schwartz S. R., Ballouz R., Bottke W. F., Campins H. and Lauretta D. S. (2020a) Thermal fatigue as a driving mechanism for asteroid activity. *Journal of Geophysical Research - Planets* **125**.

Molaro J. L., Walsh K. J., Jawin E. R., Ballouz R.-L., Bennett C. A., DellaGiustina D., Golish D. R., d'Aubigny C. D., Rizk B., Schwartz S. R., Hanna R. D., Martel S. J., Pajola M., Campins H., Ryan A. J., Bottke W. F. and Lauretta D. S. (2020b) In Situ Evidence of Thermally Induced Rock Breakdown Widespread on Bennu's Surface. *Nature Communications* **11**.

Nakamura T. (2005) Post-hydration thermal metamorphism of carbonaceous chondrites. *Journal of Mineralogical and Petrological Sciences* **100**, 260-272.

Nakamura T., Matsuoka M., Yamashita S., Sato Y., Mogi K., Enokido Y., Nakata A., Okumura S., Furukawa Y. and Zolensky M. (2017) Mineralogical, Spectral, and Compositional Changes During Heating of Hydrous Carbonaceous Chondrites. *Lunar and Planetary Science Conference XLVIII.* #1954(abstr.).

Noguchi T., Matsumoto T., Miyake A., Igami Y., Haruta M., Saito H., Hata S., Seto Y., Miyahara M., Tomioka N., Ishii H. A., Bradley J. P., Ohtaki K. K., Dobrică E., Leroux H., Le Guillou C., Jacob D., de la Peña F., Laforet S., Marinova M., Langenhorst F., Harries D., Beck P., Phan T. H. V., Rebois R., Abreu N. M., Gray J., Zega T., Zanetta P.-M., Thompson M. S., Stroud R., Burgess K., Cymes B. A., Bridges J. C., Hicks L., Lee M. R., Daly L., Bland P. A., Zolensky M. E., Frank D. R., Martinez J., Tsuchiyama A., Yasutake M., Matsuno J., Okumura S., Mitsukawa I., Uesugi K., Uesugi M., Takeuchi A., Sun M., Enju S., Takigawa A., Michikami T., Nakamura T., Matsumoto M., Nakauchi Y., Abe M., Arakawa M., Fujii A., Hayakawa M., Hirata N., Hirata N., Honda R., Honda C., Hosoda S., Iijima Y.-i., Ikeda H., Ishiguro M., Ishihara Y., Iwata T., Kawahara K., Kikuchi S., Kitazato K., Matsumoto K., Matsuoka M., Mimasu Y., Miura A., Morota T., Nakazawa S., Namiki N., Noda H., Noguchi R., Ogawa N., Ogawa K., Okada T., Okamoto C., Ono G., Ozaki M., Saiki T., Sakatani N., Sawada H., Senshu H., Shimaki Y., Shirai K., Sugita S., Takei Y., Takeuchi H., Tanaka S., Tatsumi E., Terui F., Tsukizaki R., Wada K., Yamada M., Yamada T., Yamamoto Y., Yano H., Yokota Y., Yoshihara K., Yoshikawa M., Yoshikawa K., Fukai R., Furuya S., Hatakeda K., Hayashi T., Hitomi Y., Kumagai K., Miyazaki A., Nakato A., Nishimura M., Soejima H., Suzuki A. I., Usui T., Yada T., Yamamoto D., Yogata K., Yoshitake M., Connolly H. C., Lauretta D. S., Yurimoto H., Nagashima K., Kawasaki N., Sakamoto N., Okazaki R., Yabuta H., Naraoka H., Sakamoto K., Tachibana S., Watanabe S.-i. and Tsuda Y. (2022) A dehydrated space-weathered skin cloaking the hydrated interior of Ryugu. *Nature Astronomy*.

Osterloo M. M., Hamilton V. E. and Anderson F. S. (2012) A laboratory study of the effects of roughness on the thermal infrared spectra of rock surfaces. *Icarus* **220**, 404-426.

Praet A., Barucci A., Clark B., Kaplan H., Simon A., Hamilton V., Emery J., Howell E. S., Lim L., Zou X., Li J. Y., Reuter D. C., Merlin F., Deshapriya J. D. P., Fornasier S., Hasselman P., Poggiali G., Ferrone S., Brucato J. R., Takir D., Cloutis E., Connolly Jr H. C., Fulchignoni M. and Lauretta D. (2021) Hydrogen abundance estimation and distrbution on (101955) Bennu. *Icarus* **363**.

Praet A., Poggiali G., Barucci M. A., Clark B. E., Zou X.-D., Simon A. A., Kaplan H. H., Li J.-Y. and Alcaria C. (2022) Evaluating possible spectroscopic variation of Bennu's sampling site. *Monthly Notices of the Royal Astronomical Society* **519**, 1464-1475.

Prince B. S. and Loeffler M. J. (2022) Space weathering of the 3-µm phyllosilicate feature induced by pulsed laser irradiation. *Icarus* **372**, 114736.

Ramsey M. S. and Christensen P. R. (1998) Mineral abundance determination: Quantitative deconvolution of thermal emission spectra. *J. Geophys. Res.* **103**, 577-596.

Ramsey M. S. and Fink J. H. (1999) Estimating silicic lava vesicularity with thermal remote sensing: A new technique for volcanic mapping and monitoring. *Bulletin of Volcanology* **61**, 32-39.

Reuter D. C., Simon A. A., Hair J., Lunsford A., Manthripragada S., Bly V., Bos B., Brambora C., Caldwell E., Casto G., Dolch Z., Finneran P., Jennings D., Jhabvala M., Matson E., McLelland M., Roher W., Sullivan T., Weigle E., Wen Y., Wilson D. and Lauretta D. S. (2018) The OSIRIS-REx Visible and InfraRed Spectrometer (OVIRS): Spectral Maps of the Asteroid Bennu. *Space Science Reviews* **214**, 54.

Rizk B., Drouet d'Aubigny C., Golish D., Fellows C., Merrill C., Smith P., Walker M. S., Hendershot J. E., Hancock J., Bailey S. H., DellaGiustina D. N., Lauretta D. S., Tanner R., Williams M., Harshman K., Fitzgibbon M., Verts W., Chen J., Connors T., Hamara D., Dowd A., Lowman A., Dubin M., Burt R., Whiteley M., Watson M., McMahon T., Ward M., Booher D., Read M., Williams B., Hunten M., Little E., Saltzman T., Alfred D., O'Dougherty S., Walthall M., Kenagy K., Peterson S., Crowther B., Perry M. L., See C., Selznick S., Sauve C., Beiser M., Black W., Pfisterer R. N., Lancaster A., Oliver S., Oquest C., Crowley D., Morgan C., Castle C., Dominguez R. and Sullivan M. (2018) OCAMS: The OSIRIS-REx Camera Suite. *Space Science Reviews* **214**, 26.

Rozitis B., Ryan A. J., Emery J. P., Christensen P. R., Hamilton V. E., Simon A. A., Reuter D. C., Al Asad M., Ballouz R. L., Bandfield J. L., Barnouin O. S., Bennett C. A., Bernacki M., Burke K. N., Cambioni S., Clark B. E., Daly M. G., Delbo M., DellaGiustina D. N., Elder C. M., Hanna R. D., Haberle C. W., Howell E. S., Golish D. R., Jawin E. R., Kaplan H. H., Lim L. F., Molaro J. L., Munoz D. P., Nolan M. C., Rizk B., Siegler M. A., Susorney H. C. M., Walsh K. J. and Lauretta D. S. (2020) Asteroid (101955) Bennu's weak boulders and thermally anomalous equator. *Science Advances* **6**, eabc3699.

Salisbury J. W. (1993) Mid-infrared spectroscopy: Laboratory data. In *Remote Geochemical Analysis: Elemental and Mineraliogical Composition* (eds. C.M. Pieters and P.A.J. Englert). Cambridge University Press, New York. pp. 79-98 (Ch. 74).

Sasaki S., Nakamura K., Hamabe Y., Kurahashi E. and Hiroi T. (2001) Production of iron nanoparticles by laser irradiation in a simulation of lunar-like space weathering. *Nature* **410**, 555-557.

Sidhu S., Cloutis E. A., Mann P., Applin D., Hiroi T., Mengel K., Kareta T., Reddy V., Beck P. and Mertzman S. A. (2023) Spectral and mineralogical effects of heating on CM chondrite and related asteroids. *Icarus* **398**, 115522.

Simon A. A., Kaplan H. H., Cloutis E., Hamilton V. E., Lantz C., Reuter D. C., Trang D., Fornasier S., Clark B. E. and Lauretta D. S. (2020a) Weak spectral features on (101995) Bennu from the OSIRIS-REx Visible and InfraRed Spectrometer. *A&A* **644**.

Simon A. A., Kaplan H. H., Hamilton V. E., Lauretta D. S., Campins H., Emery J. P., Barucci M. A., DellaGiustina D. N., Reuter D. C., Sandford S. A., Golish D. R., Lim L. F., Ryan A., Rozitis B. and Bennett C. A. (2020b) Widespread carbon-bearing materials on near-Earth asteroid (101955) Bennu. *Science* **370**, eabc3522.

Simon A. A., Reuter D. C., Gorius N., Lunsford A., Cosentino R. G., Wind G., Lauretta D. S. and The O.-R. T. (2018). *In-Flight Calibration and Performance of the OSIRIS-REx Visible and IR Spectrometer (OVIRS)*, Remote Sensing.

Thompson M. S., Loeffler M. J., Morris R. V., Keller L. P. and Christoffersen R. (2019) Spectral and chemical effects of simulated space weathering of the Murchison CM2 carbonaceous chondrite. *Icarus* **319**, 499-511.

Thompson M. S., Morris R. V., Clemett S. J., Loeffler M. J., Trang D., Keller L. P., Christoffersen R. and Agresti D. G. (2020) The effect of progressive space weathering on the organic and inorganic components of a carbonaceous chondrite. *Icarus* **346**, 113775.

Tonui E., Zolensky M., Hiroi T., Nakamura T., Lipschutz M. E., Wang M.-S. and Okudaira K. (2014) Petrographic, chemical and spectroscopic evidence for thermal metamorphism in carbonaceous chondrites I: CI and CM chondrites. *Geochim. Cosmoch. Acta* **126**, 284-306.

Trang D., Thompson M. S., Clark B. E., Kaplan H. H., Zou X.-D., Li J.-Y., Ferrone S. M., Hamilton V. E., Simon A. A., Reuter D. C., Keller L. P., Barucci M. A., Campins H., Lantz C., DellaGiustina D. N., Ballouz R.-L., Jawin E. R., Connolly H. C., Walsh K. J. and Lauretta D. S. (2021) The Role of Hydrated Minerals and Space Weathering Products in the Bluing of Carbonaceous Asteroids. *The Planetary Science Journal* **2**, 68.

Velbel M. A. and Zolensky M. E. (2021) Thermal metamorphism of CM chondrites: A dehydroxylation-based peak-temperature thermometer and implications for sample return from asteroids Ryugu and Bennu. *Meteoritics & Planetary Science* **56**, 546-585.

Vernazza P., Binzel R. P., Rossi A., Fulchignoni M. and Birlan M. (2009) Solar wind as the origin of rapid reddening of asteroid surfaces. *Nature* **458**, 993-995.

Vincent R. K. and Hunt G. R. (1968) Infrared reflectance from mat surfaces. *Applied Optics* **7**, 53-59.

Walsh K. J., Jawin E. R., Ballouz R. L., Barnouin O. S., Bierhaus E. B., Connolly H. C., Molaro J. L., McCoy T. J., Delbo' M., Hartzell C. M., Pajola M., Schwartz S. R., Trang D., Asphaug E., Becker K. J., Beddingfield C. B., Bennett C. A., Bottke W. F., Burke K. N., Clark B. C., Daly M. G., DellaGiustina D. N., Dworkin J. P., Elder C. M., Golish D. R., Hildebrand A. R., Malhotra R., Marshall J., Michel P., Nolan M. C., Perry M. E., Rizk B., Ryan A., Sandford S. A., Scheeres D. J., Susorney H. C. M., Thuillet F., Lauretta D. S., Highsmith D. E., Small J., Vokrouhlický D., Bowles N. E., Brown E., Donaldson Hanna K. L., Warren T., Brunet C., Chicoine R. A., Desjardins S., Gaudreau D., Haltigin T., Millington-Veloza S., Rubi A., Aponte J., Gorius N., Lunsford A., Allen B., Grindlay J., Guevel D., Hoak D., Hong J., Schrader D. L., Bayron J., Golubov O., Sánchez P., Stromberg J., Hirabayashi M., Hartzell C. M., Oliver S., Rascon M., Harch A., Joseph J., Squyres S., Richardson D., Emery J. P., McGraw L., Ghent R., Binzel R. P., Al Asad M. M., Johnson C. L., Philpott L., Susorney H. C. M., Cloutis E. A., Hanna R. D., Connolly H. C., Ciceri F., Hildebrand A. R., Ibrahim E. M., Breitenfeld L., Glotch T., Rogers A. D., Clark B. E., Ferrone S., Thomas C. A., Campins H., Fernandez Y., Chang W., Cheuvront A., Trang D., Tachibana S., Yurimoto H., Brucato J. R., Poggiali G., Pajola M., Dotto E., Epifani E. M., Crombie M. K., Lantz C., Izawa M. R. M., de Leon J., Licandro J., Garcia J. L. R., Clemett S., Thomas-Keprta K., Van wal S., Yoshikawa M., Bellerose J., Bhaskaran S., Boyles C., Chesley S. R., Elder C. M., Farnocchia D., Harbison A., Kennedy B., Knight A., Martinez-Vlasoff N., Mastrodemos N., McElrath T., Owen W., Park R., Rush B., Swanson L., Takahashi Y., Velez D., Yetter K., Thayer C., Adam C., Antreasian P., Bauman J., Bryan C., Carcich B., Corvin M., Geeraert J., Hoffman J., Leonard J. M., Lessac-Chenen E., Levine A., McAdams J., McCarthy L., Nelson D., Page B., Pelgrift J., Sahr E., Stakkestad K., Stanbridge D., Wibben D., Williams B., Williams K., Wolff P., Hayne P., Kubitschek D., Barucci M. A., Deshapriya J. D. P., Fornasier S., Fulchignoni M., Hasselmann P., Merlin F., Praet A., Bierhaus E. B., Billett O., Boggs A., Buck B., Carlson-Kelly S., Cerna J., Chaffin K., Church E., Coltrin M., Daly J., Deguzman A., Dubisher R., Eckart D., Ellis D., Falkenstern P., Fisher A., Fisher M. E., Fleming P., Fortney K., Francis S., Freund S., Gonzales S., Haas P., Hasten A., Hauf D., Hilbert A., Howell D., Jaen F., Jayakody N., Jenkins M., Johnson K., Lefevre M., Ma H., Mario C., Martin K., May C., McGee M., Miller B., Miller C., Miller G., Mirfakhrai A., Muhle E., Norman C., Olds R., Parish C., Ryle M., Schmitzer M., Sherman P., Skeen M., Susak M., Sutter B., Tran Q., Welch C., Witherspoon R., Wood J., Zareski J., Arvizu-Jakubicki M., Asphaug E., Audi E., Ballouz R. L., Bandrowski R., Becker K. J., Becker T. L., Bendall S., Bennett C. A., Bloomenthal H., Blum D., Boynton W. V., Brodbeck J., Burke K. N., Chojnacki M., Colpo A., Contreras J., Cutts J., Drouet d'Aubigny C. Y., Dean D., DellaGiustina D. N., Diallo B., Drinnon D., Drozd K., Enos H. L., Enos R., Fellows C., Ferro T., Fisher M. R., Fitzgibbon G., Fitzgibbon M., Forelli J., Forrester T., Galinsky I., Garcia R., Gardner A., Golish D. R., Habib N., Hamara D., Hammond D., Hanley K., Harshman K., Hergenrother C. W., Herzog K., Hill D., Hoekenga C., Hooven S., Howell E. S., Huettner E., Janakus A., Jones J., Kareta T. R., Kidd J., Kingsbury K., Balram-Knutson S. S., Koelbel L., Kreiner J., Lambert D., Lauretta D. S., Lewin C., Lovelace B., Loveridge M., Lujan M., Maleszewski C. K., Malhotra R., Marchese K., McDonough E., Mogk N., Morrison V., Morton E., Munoz R., Nelson J., Nolan M. C., Padilla J., Pennington R., Polit A. and The O.-R. T. (2019) Craters, boulders and regolith of (101955) Bennu indicative of an old and dynamic surface. *Nature Geoscience* **12**, 242-246.

Zhang P., Tai K., Li Y., Zhang J., Lantz C., Hiroi T., Matsuoka M., Li S., Lin Y., Wen Y., Han H. and Zeng X. (2022) Diverse space weathering effects on asteroid surfaces as inferred via laser irradiation of meteorites. *A&A* **659**, A78.

Zolensky M., Barrett R. and Browning L. (1993) Mineralogy and composition of matrix and chondrule rims in carbonaceous chondrites. *Geochim. Cosmoch. Acta* **57**, 3123-3148.

Zolensky M. E., Nakamura K., Gounelle M., Mikouchi T., Kasama T., Tachikawa O. and Tonui E. (2002) Mineralogy of Tagish Lake: An ungrouped type 2 carbonaceous chondrite. *Meteoritics & Planetary Science* **37**, 737-761.

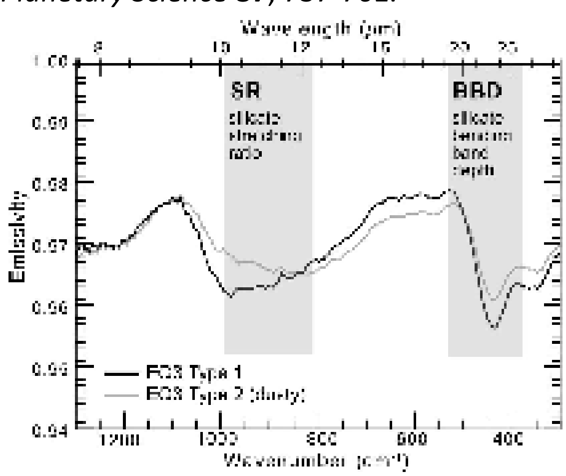

Figure 1. OTES EQ3 Types 1 and 2 defined by the silicate stretching ratio (SR) (Hamilton et al. 2021). Standard errors are shown as vertical lines and are on the scale of the line width in many cases. Type 2 spectrum is interpreted to have a higher component of optically thin or patchy dust, with a higher SR as well as a shallower silicate bending band depth (BBD). Grey boxes show wavelength areas used to define SR and BBD indices.

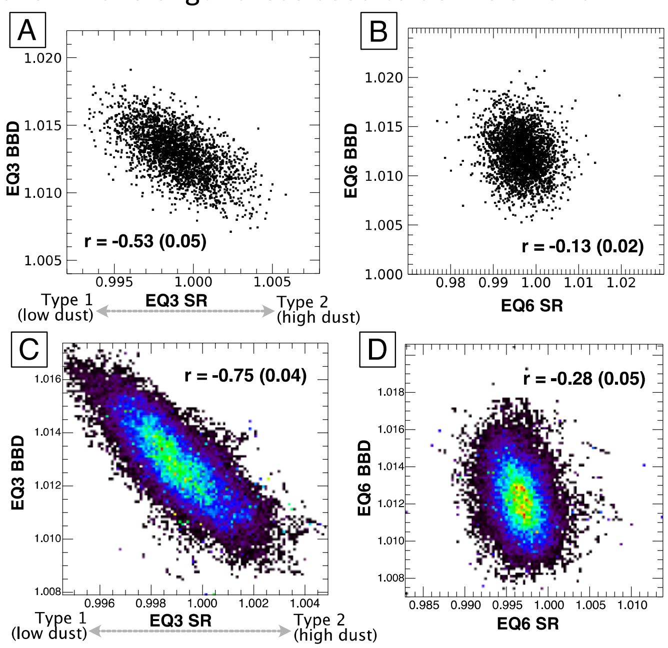

Figure 2. Si-O stretching ratios (SRs) plotted against the 440 cm^{-1} band depth (BBD). EQ3 (12:30 pm) data on left (A,C) and EQ6 (8:40 pm) data on right (B,D). A and B are scatter plots of individual spectra (A: n = 2558; B: n=2788) and C and D are density plots (warmer colors represent denser data) of weighted averaged values combined on a per-facet basis on a 50K shape model of Bennu (n = 49,152). During the day, the SR is correlated to the BBD but this correlation disappears at night as the relative radiation from thin and/or patchy dust on Bennu is minimized.

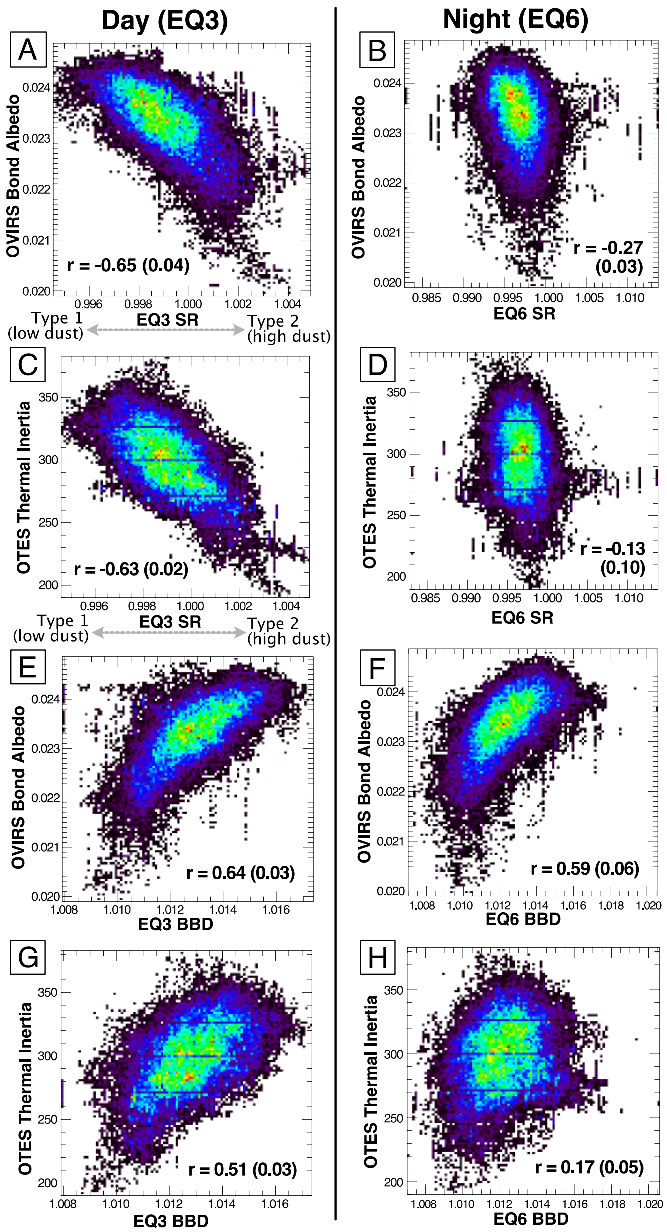

Figure 3. (A-D) Density plots of the SR from EQ3 (12:30 pm; A,C) and EQ6 (8:40 pm; B,D) plotted with OVIRS bond albedo (A,B), OTES thermal inertia (C,D). (E-H) Density plots of BBD from EQ3 (12:30 pm; E,G) and EQ6 (8:40 pm; F,H) plotted with OVIRS bond albedo (E,F) and OTES thermal inertia (G,H). Horizontal lines in the OTES thermal inertia density plots are an artifact of the dataset resolution. The SR is strongly correlated to Bennu's albedo and thermal inertia but correlations disappear at night when the radiance of dust is minimal. The BBD is strongly correlated to Bennu's daytime albedo and moderately correlated to daytime thermal inertia. At night, the correlation of the BBD with thermal inertia is gone, but correlation to albedo remains.

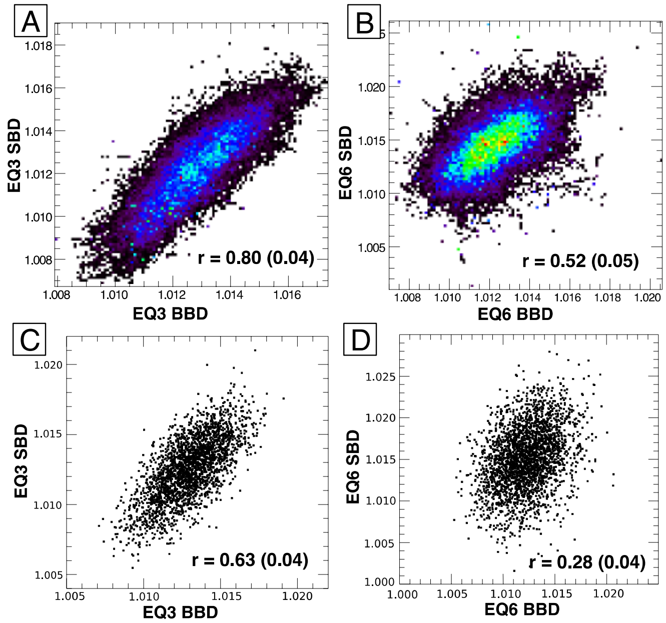

Figure 4. (A,B) Density plot of Si-O bending band depth (BBD) and stretching band depth (SBD) from EQ3 (12:30 pm; A) and EQ6 (8:40 pm; B). Daytime band depths are strongly correlated due to the radiance of dust which decreases both band depths in tandem. The moderate nighttime band depth correlation (B) suggests dust radiance, or particle size or roughness variations may be an influence at night. However, for individual OTES spectra, the Si-O stretching and bending band depths are only correlated during the day (C), due to the dust radiance.

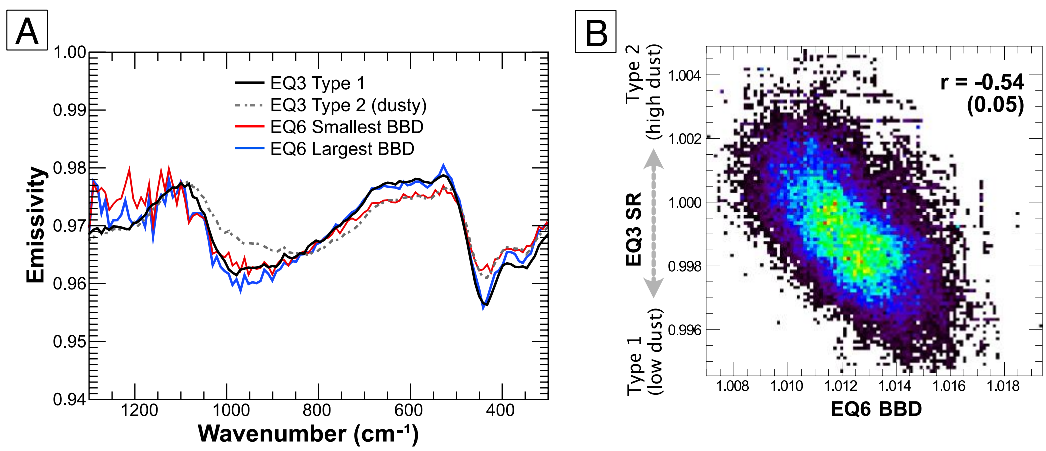

Figure 5. (A) Low and high dust spectral types of Hamilton et al. 2001 defined by the average of the 100 EQ3 (12:30 pm) spectra having the highest and lowest Si-O stretching ratios, respectively, plotted with the averages of the 300 EQ6 (8:40 pm) spectra having the largest and smallest 440 cm^{-1} band depths, named low and high BBD, respectively. Standard errors are shown as vertical lines and are on the scale of the line width in many cases. The Si-O stretching shape of both BBD spectra are similar to the Type 1 (minimal dust) spectra while their 440 cm^{-1} band depths are different. (B) Density plot of the EQ3 SR and the EQ6 BBD showing a moderate negative correlation.

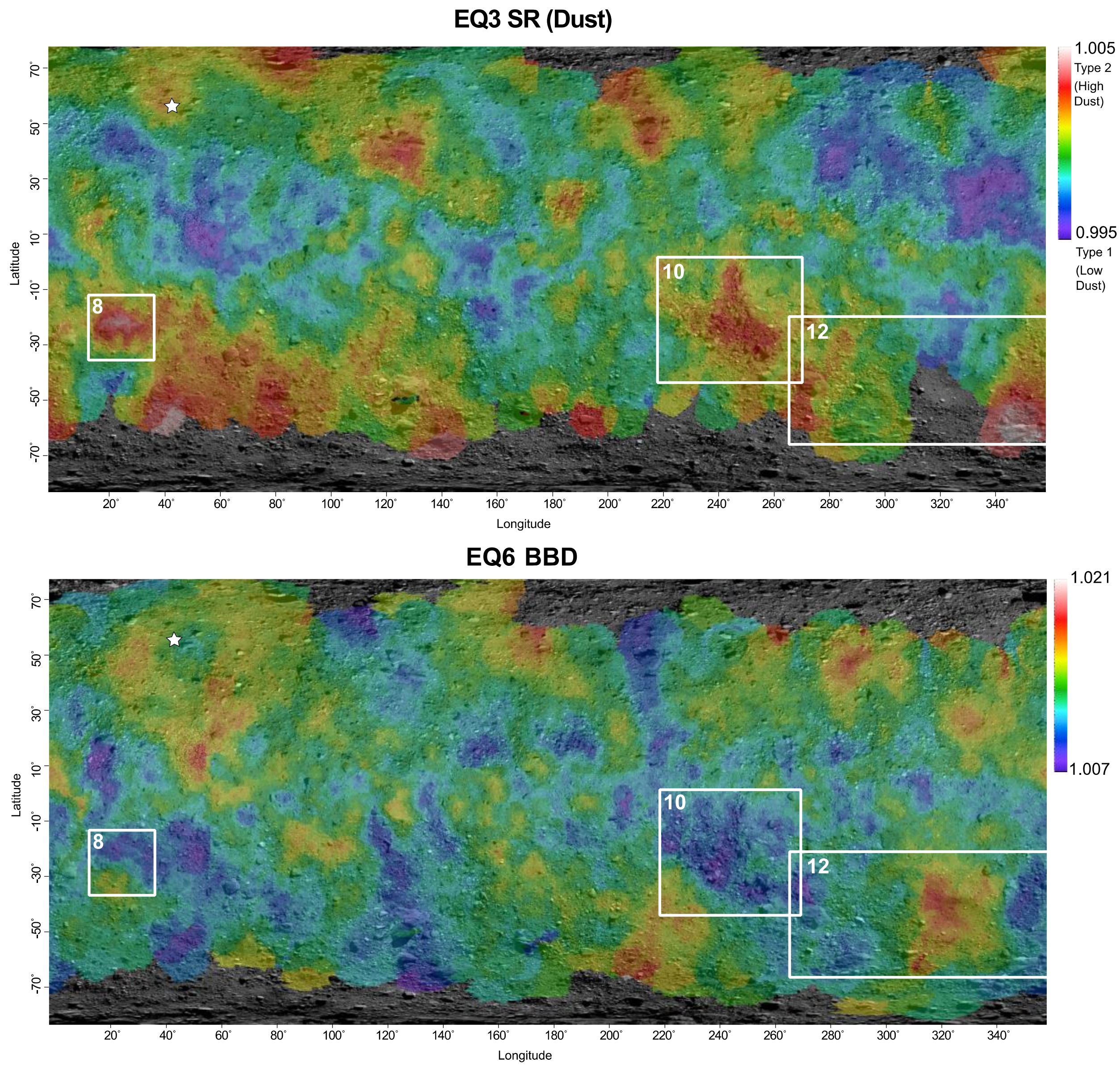

Figure 6. (Top) Map of spectral EQ3 SR (Types 1 and 2 of Hamilton et al. 2021) (Bottom) Map of EQ6 BBD. White star denotes the Nightingale sampling site, and the boxes and numbers refer to areas examined in the designated figure.

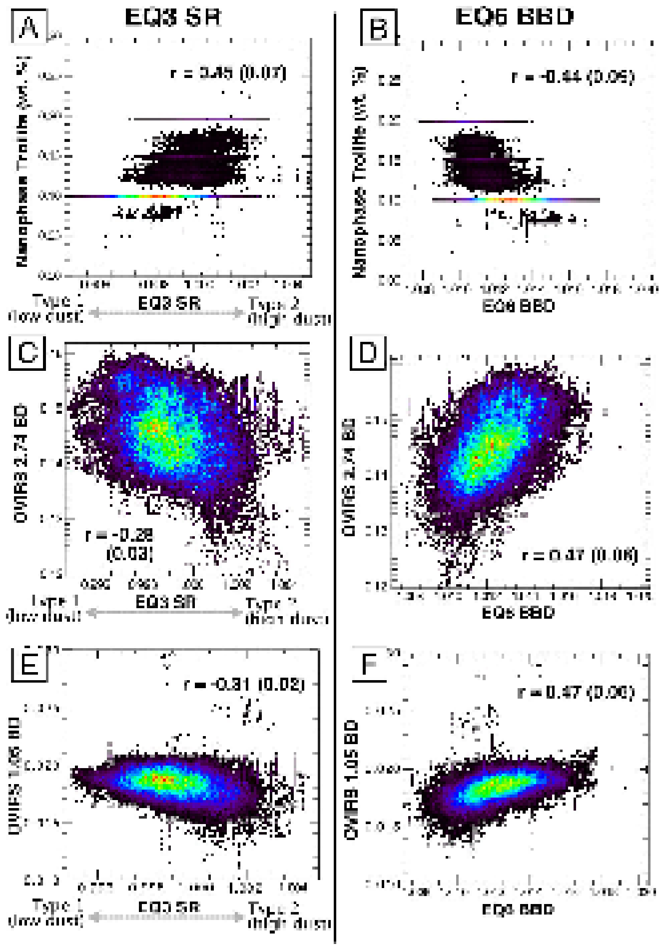

Figure 7. Density plots of the EQ3 SR (left plots) and the EQ6 BBD (right plots) versus OVIRS-derived data products. Horizontal striping in (A) and (B) is an artifact due to data resolution of the troilite map of Trang et. al (2021). Both OTES indices appear moderately correlated with nanophase troilite abundance (A,B), but only EQ6 BBD correlated to OVIRS 2.74 and 1.05 µm band depths

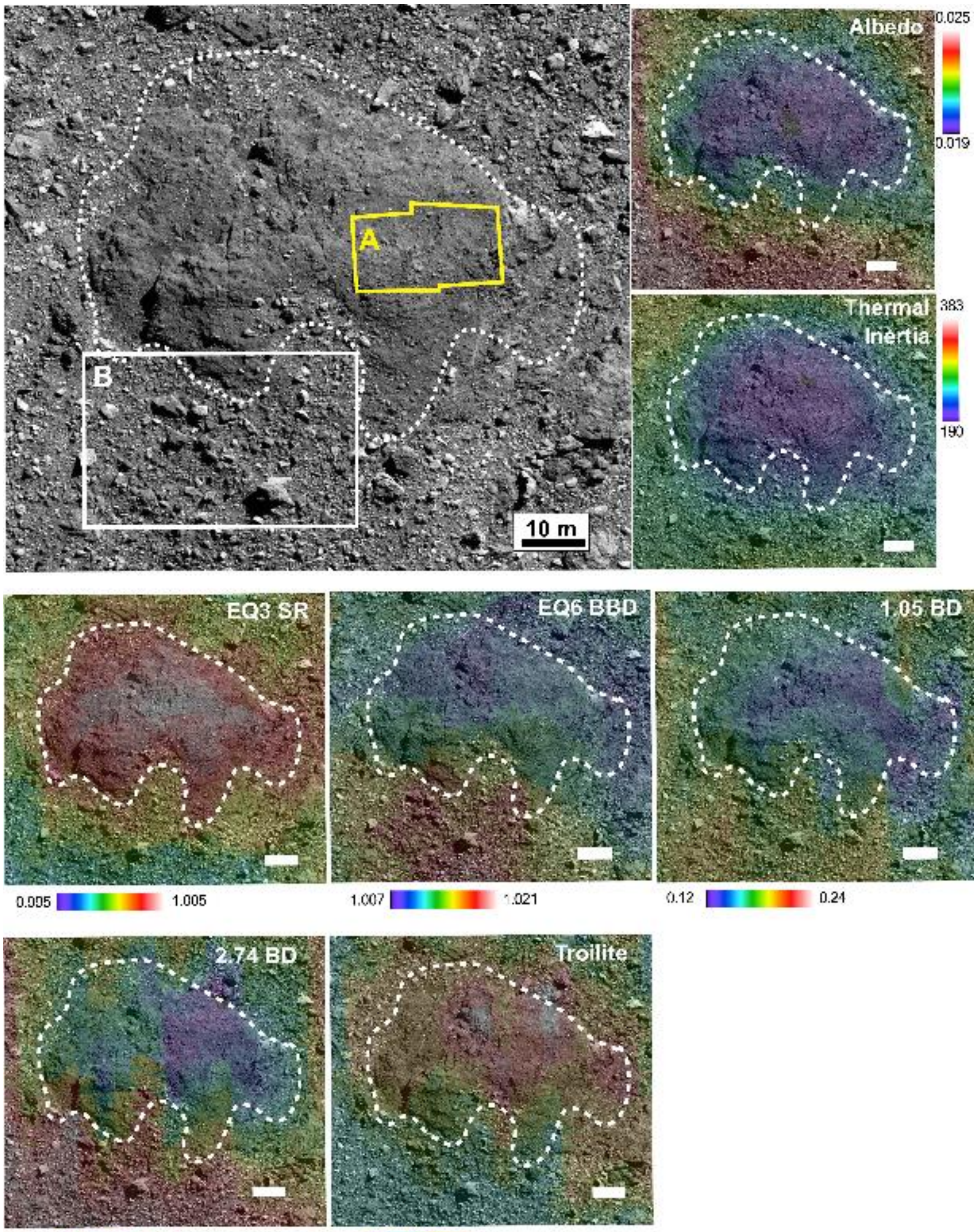

Figure 8. Large partially exposed boulder with low albedo and thermal inertia with very high EQ SR. White dashed outline shows area of highest EQ3 SR values. All scale bars 10 m, yellow and

white boxes in top PolyCam image mosaic shows the location of Figure 9. The EQ3 SR values are collocated with thermal inertia and albedo, while EQ6 BBD, 1.05 µm band depth, 2.74 µm band depth, and troilite abundance vary over the boulder surface. The northern portion of the boulder generally has lower EQ6 BBD, lower 1.05 µm and 2.74 µm band depths, and higher troilite abundance. The area to the south of the boulder (white box labeled B in PolyCam mosaic) has relatively higher EQ6 BBD, 1.05 µm and 2.74 µm band depths, and lower troilite abundance, compared to the majority of the boulder surface.

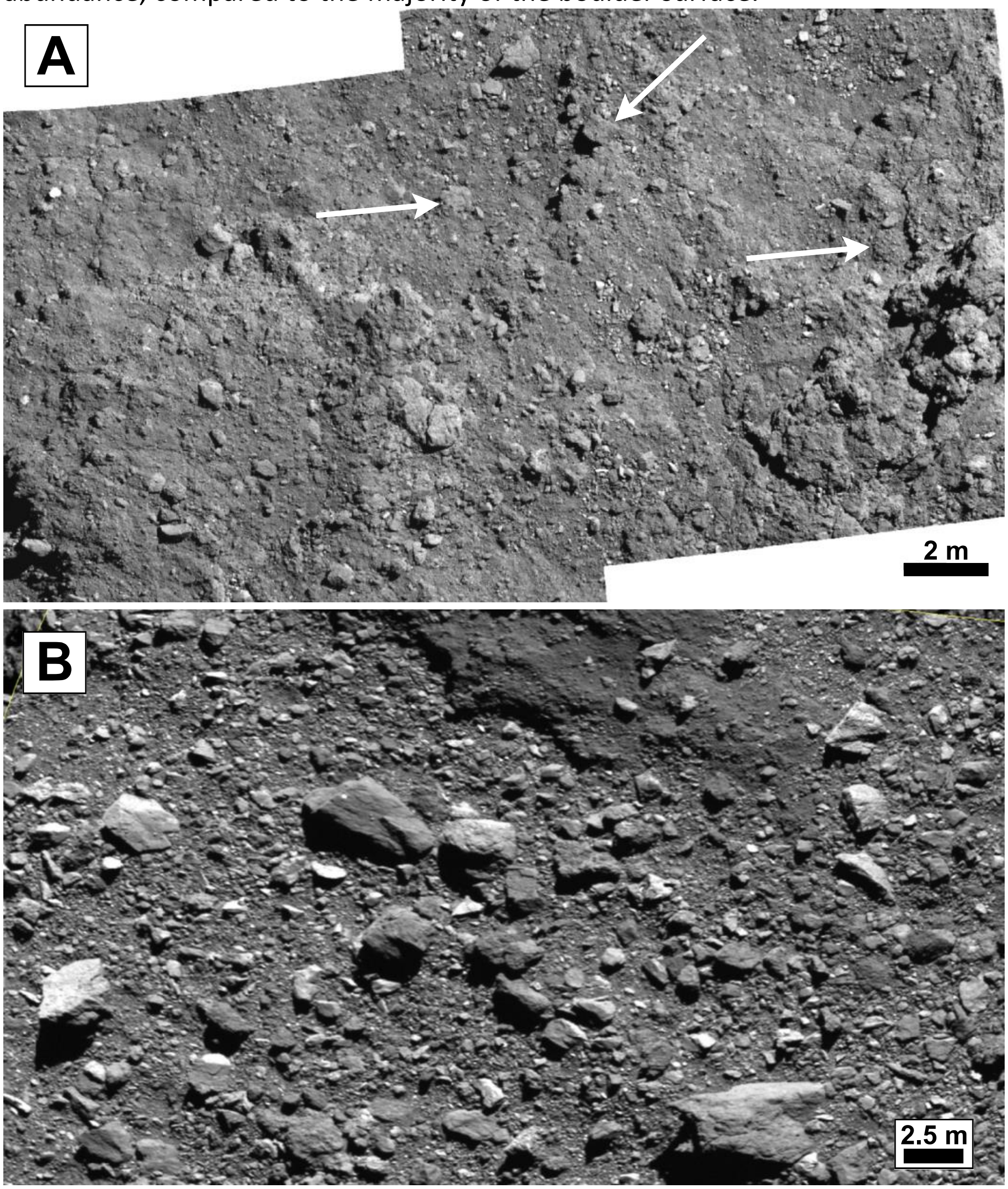

Figure 9. (A) PolyCam images 200542 and 200543 over breccia boulder (Fig. 8) showing relatively smooth surface with curvilinear fractures and partially exhumed clasts (white arrows). (B) PolyCam image 38378 over area south of boulder (Fig. 8) with relatively high EQ6 BBD and 2.74 µm band depths and low troilite abundance relative to the boulder surface. This area is composed of smaller rocks and some unresolved areas.

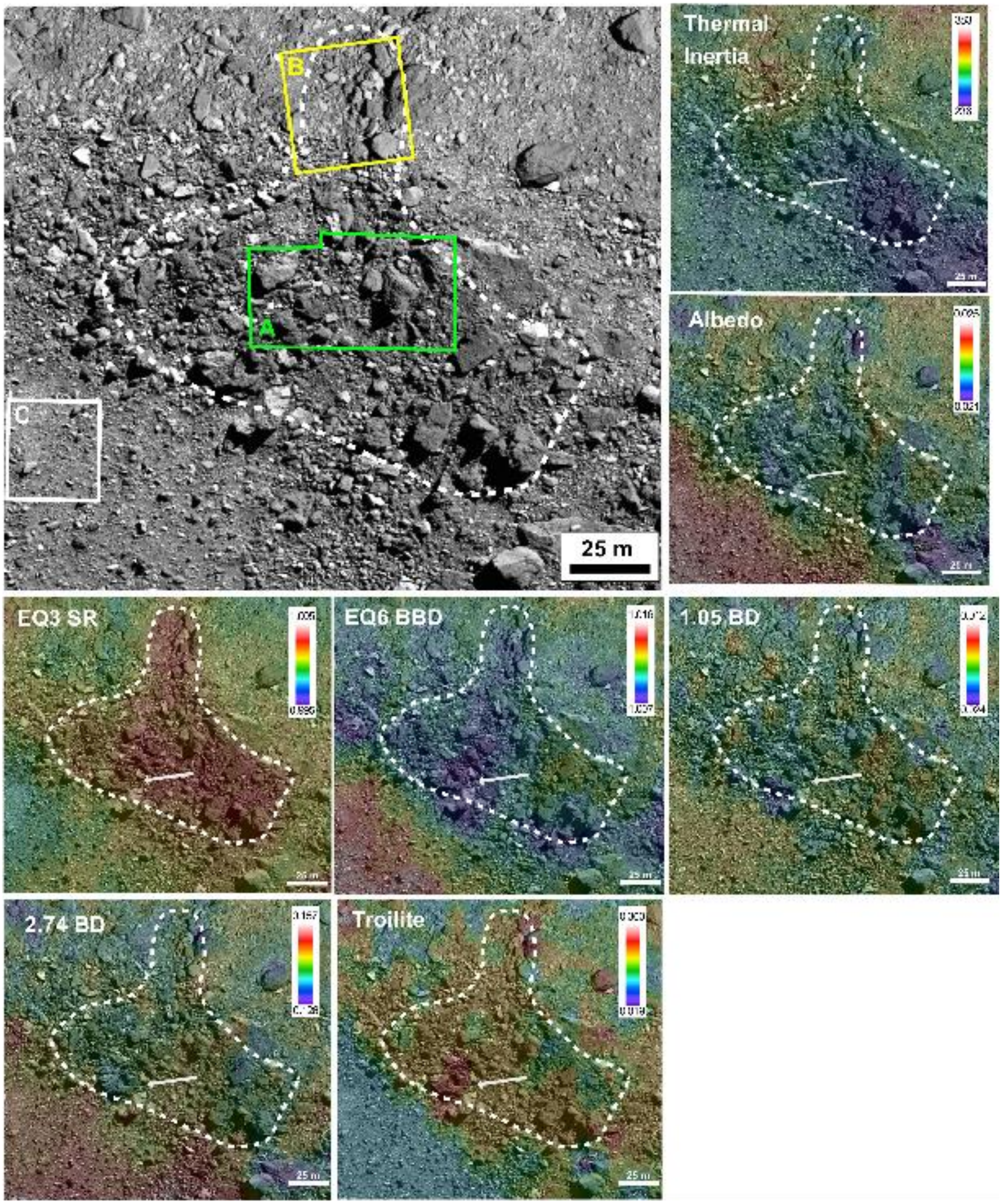

Figure 10. Boulder rich, dusty (Type 2) region. White dashed outline highlights area of the highest Si-O stretching ratio (EQ3 SR) values. White arrow points to area of relatively low EQ6 BBD, 1.05 µm and 2.74 µm band depths, and high troilite abundance. All scale bars 25 m, and colored boxes in top left PolyCam image mosaic shows the location of images in Figure 11 (green,11A; yellow, 11B; white, 11C).

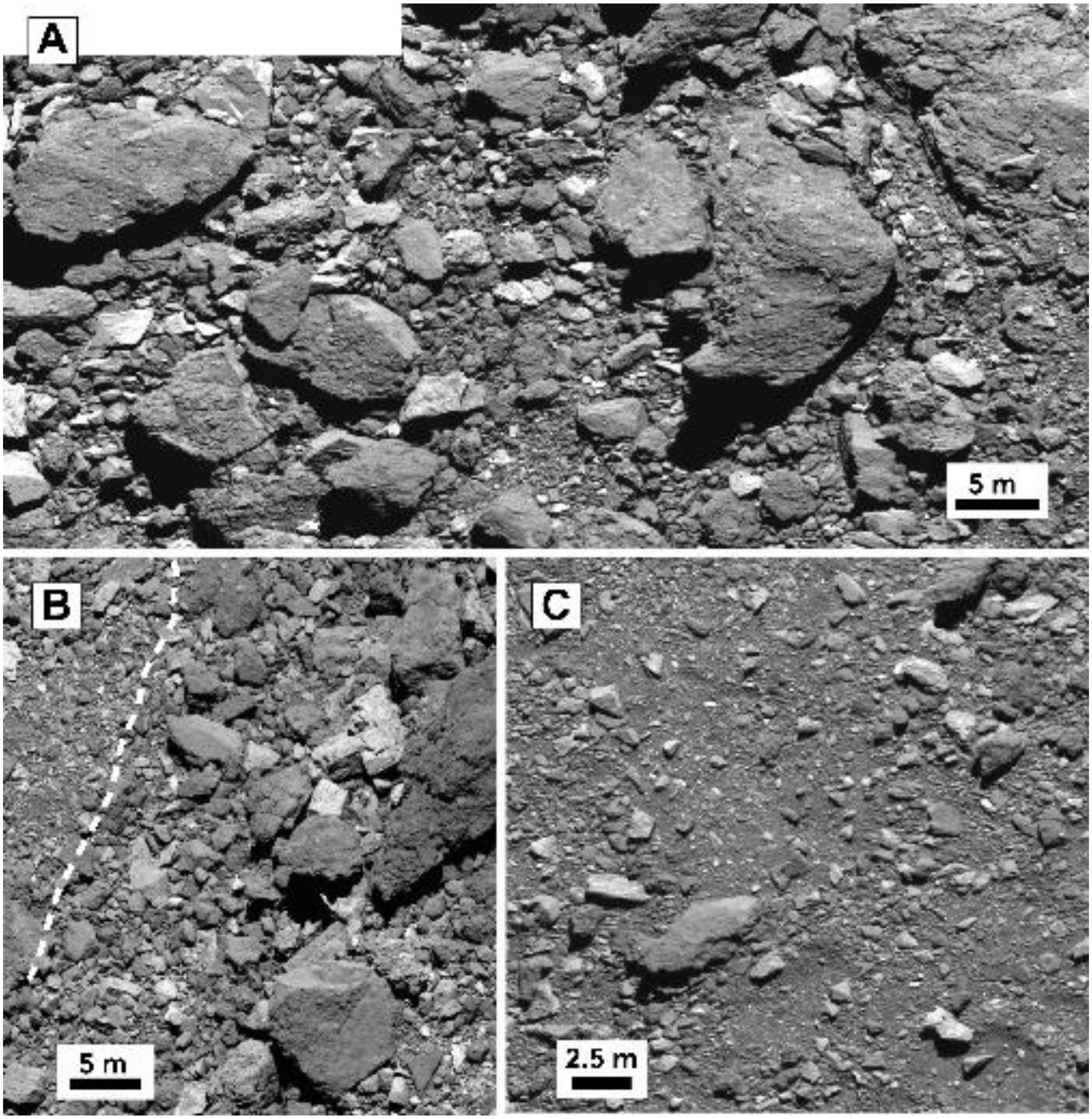

Figure 11. PolyCam images over the boulder rich region shown in Figure 10. A) PolyCam images 39086 and 39102 over the area with highest EQ3 SR values. Area is dominated by large breccia boulders and most rocks are resolvable. B) PolyCam image 39090 showing approximate boundary (white dashed line) between higher EQ3 SR values (right) and lower values (left). Area on right is characterized by larger rocks and boulders, some of which are visible breccias, while area on left contains much smaller rocks and some unresolved areas. C) PolyCam image 39158 over area with relatively low EQ3 SR values. Note scale is smaller than A and B and there is abundant unresolved material with small rocks.

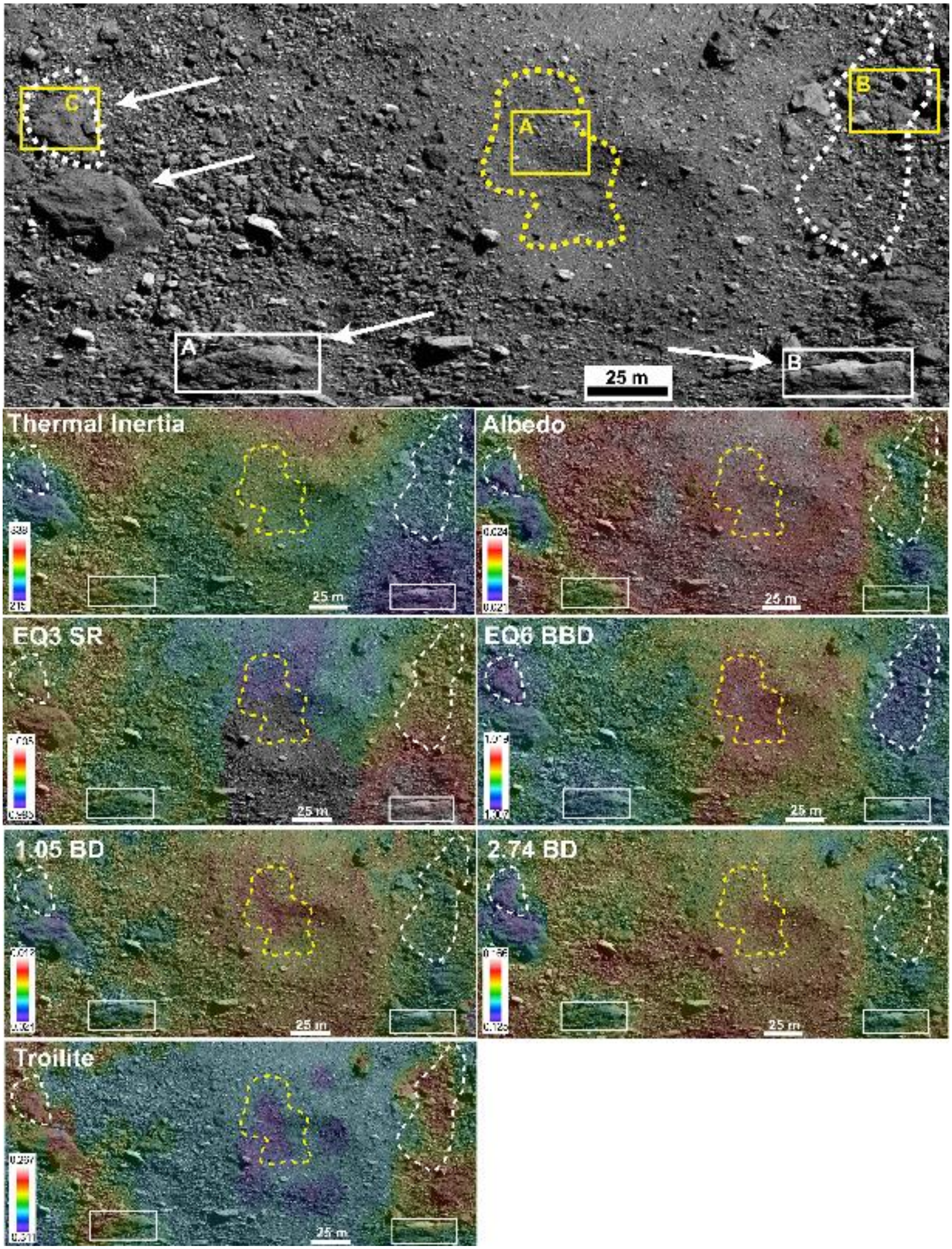

Figure 12. Region with large areas of low and high EQ6 BBD. White dashed outline highlights two areas of with smallest EQ6 BBD, and the yellow dashed line is an area with the largest EQ6

BBD. White arrows point to four large boulders discussed in text. Yellow boxes show the location of PolyCam images in Figure 13. The white boxes highlight two large boulders with similar EQ6 BBD values, 1.05 µm and 2.74 µm band depths, troilite abundances, and albedos, but with markedly different thermal inertias and EQ3 SR values, and location of PolyCam images in Figure 14. There is a gap in OTES coverage for EQ3 near the center of the region.

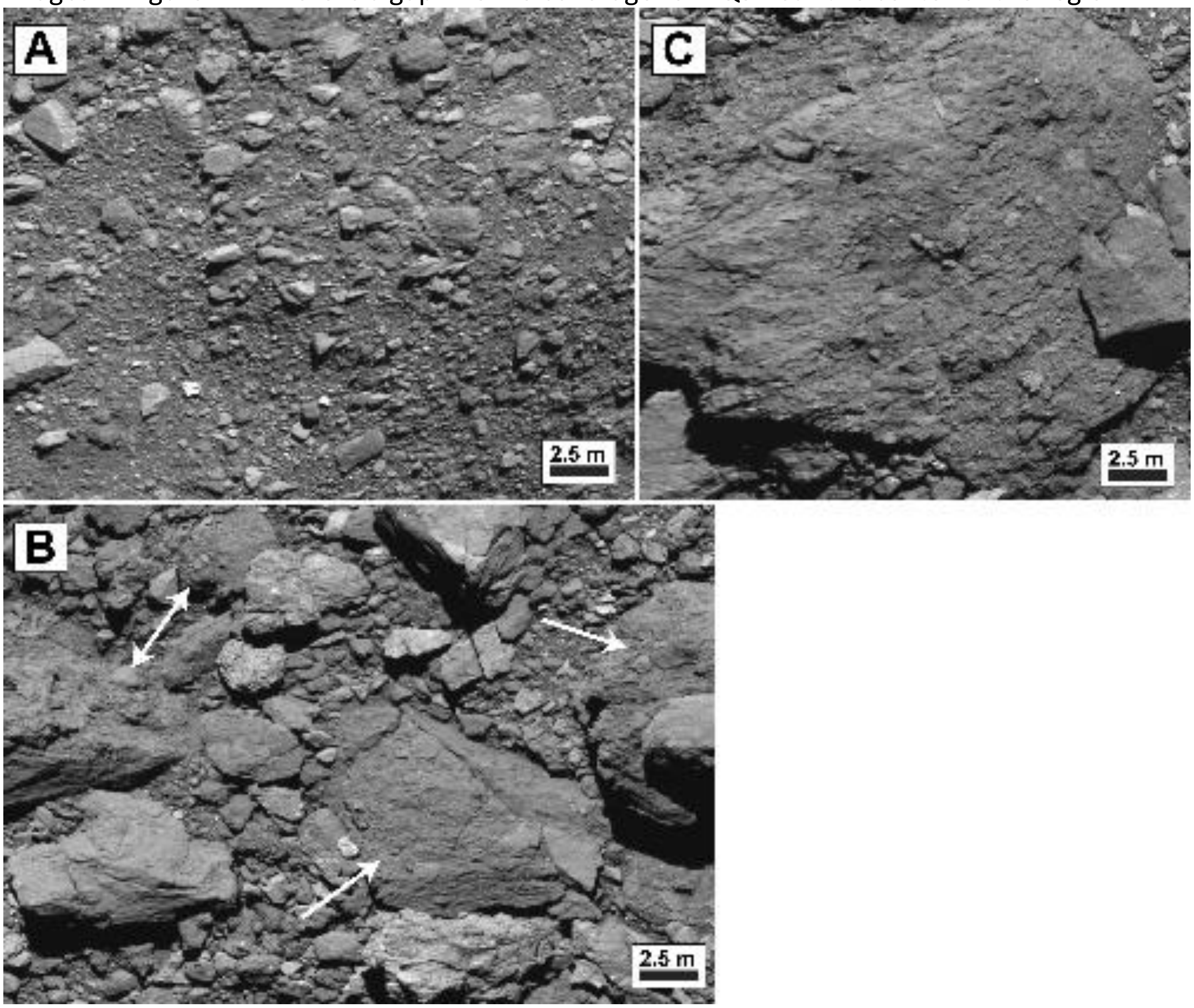

Figure 13. PolyCam images in region shown in Figure 12. A) PolyCam image 38872 over the area with largest EQ6 BBD values. Area is dominated by small bright rocks and unresolved material. B) PolyCam image 38787 over area with small EQ6 BBD values and that has larger rocks and boulders compare to area in (A), many of which are breccias (white arrows). C) PolyCam image 39016 over large boulder with small EQ6 BBD. This brecciated boulder has a distinctively low albedo, low thermal inertia, low hydration (small 2.74 µm band depths), and relatively high troilite abundance. All images have same spatial scale.

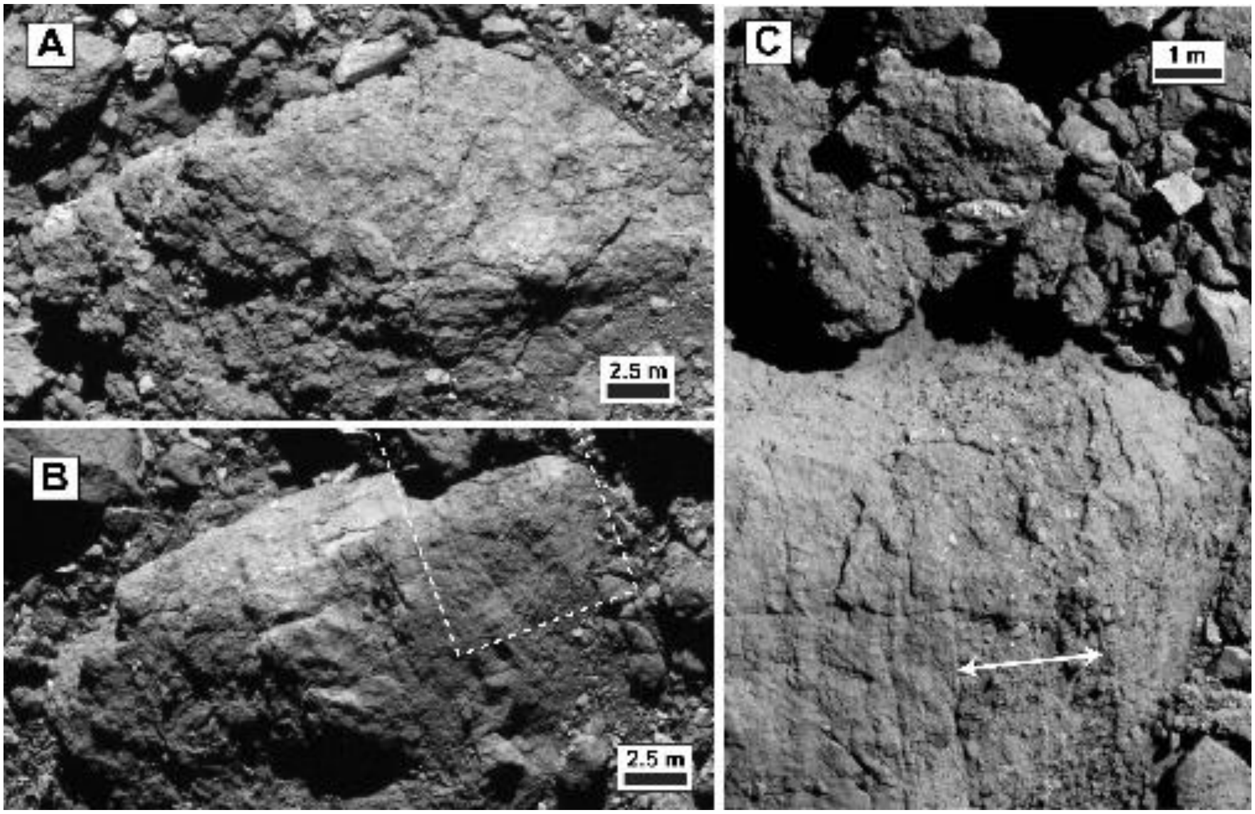

Figure 14. PolyCam images over two southern boulders shown in Figure 12. Both boulders have similar EQ6 BBD values, hydration level, albedo, and troilite abundance. A) PolyCam image 38967 over western boulder with higher thermal inertia and lower EQ3 SR values. Boulder appears brecciated with embedded clasts. B) PolyCam image 41210 over eastern boulder with much lower thermal inertia and higher EQ3 SR values (i.e., dust). Boulder is layered, and white dashed line is approximate location of higher resolution PolyCam image shown in C. C) PolyCam image 90238 eastern boulder showing layering (approximately orientated top to bottom in image) with a large layer of highly clastic material (white arrow).

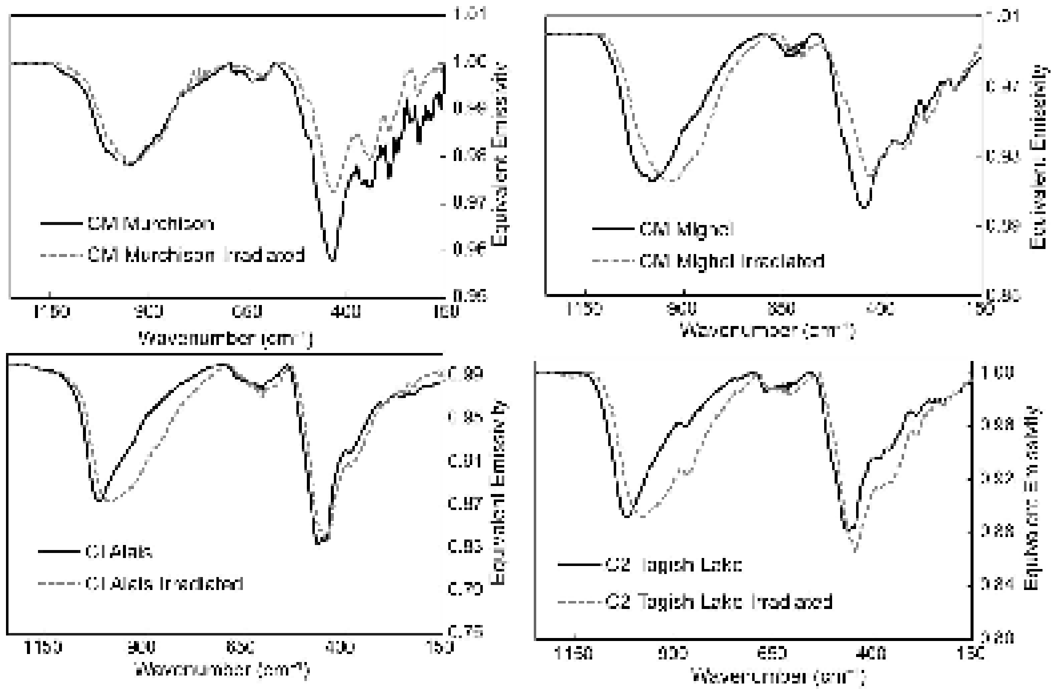

Figure 15. Data of mid- to far-infrared spectra of unirradiated (black solid) and irradiated (grey dashed) hydrated carbonaceous chondrites from Brunetto et al. (2020). Each set of spectra (unirradiated and irradiated) have been normalized so the SiO stretching depths are approximately the same. In CM-type carbonaceous chondrites the SiO bending band depth decreases relative to the SiO stretching band depth after irradiation. For CI Alais the depths remain approximately the same, and for ungrouped C2 Tagish Lake, the silicate bending band depth increases after irradiation.

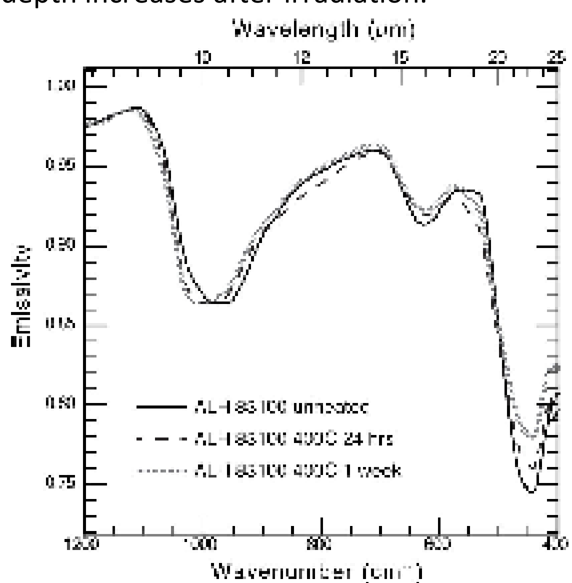

Figure 16. IR spectra of unheated and heated chips of ALH 83100. Spectra are scaled and offset to highlight the shallowing of the Si-O bending band near 440 cm^{-1} while the Si-O stretching band depth is unaffected. The Mg-OH band near 625 cm^{-1} also slightly decreases in depth with heating.

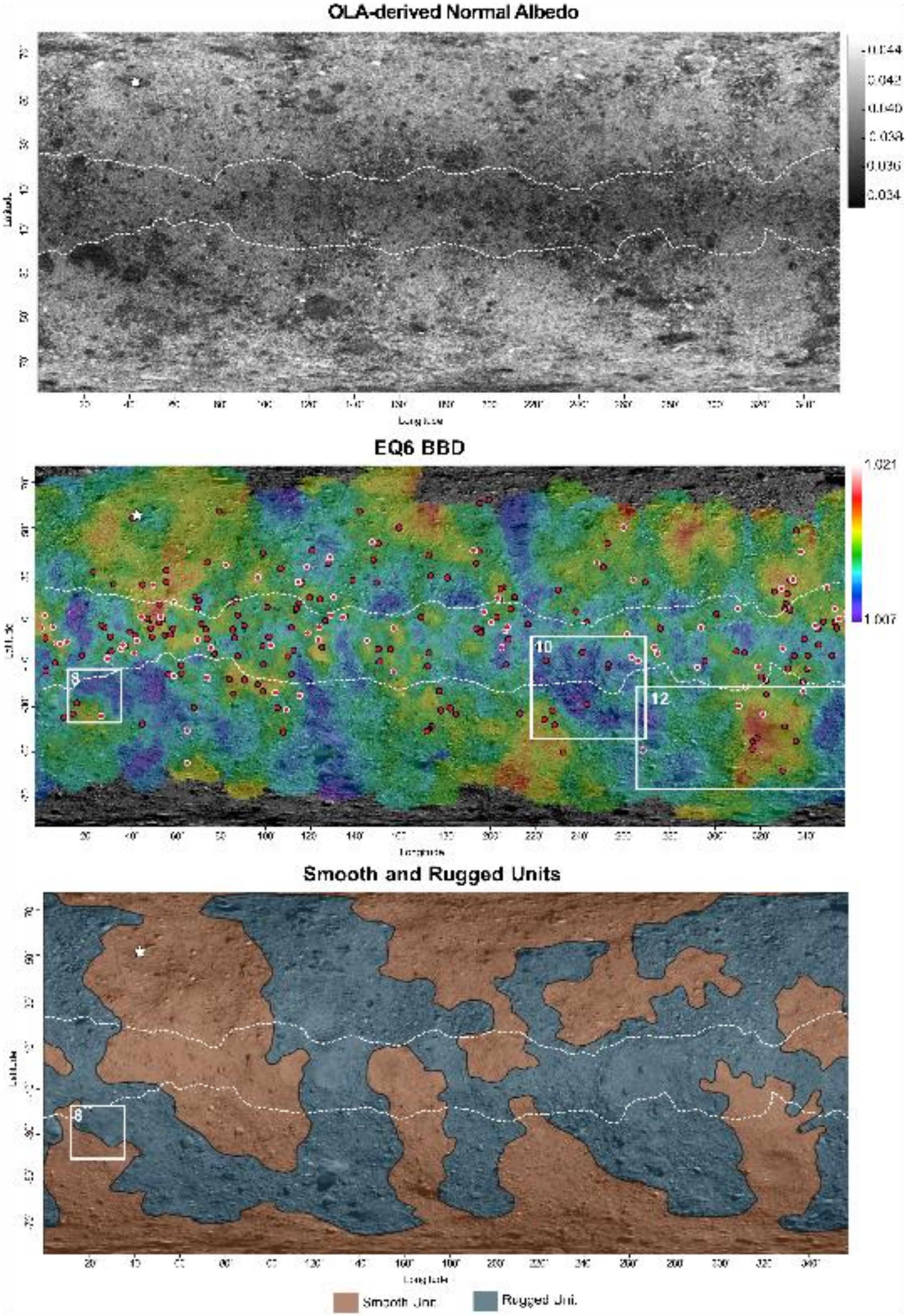
OLA-derived Normal Albedo
0.044
0.042
0.040
0.038
0.036
0.034
EQ6 BBD
1.021
1.007
10
12
8
Smooth and Rugged Units
8
Smooth Unit
Rugged Unit

Figure 17. Maps of OLA-derived normal albedo at 1064 nm (Clark et al., 2023) (top), EQ6 BBD (middle), and the Smooth and Rugged Units of Jawin et al. (2022) (bottom). The equatorial bulge as mapped by Jawin et al. (2022) is overlain on all maps and the white star (all maps) denotes the Nightingale sampling site within Hokioi crater. The map of EQ6 BBD is overlain with the reddest (youngest) craters of DellaGiustina et al. (2020) and Jawin et al. (2022). White outlined craters are the reddest (youngest) population defined by 1σ (N = 79), the remaining red craters are 0.5σ (N = 255) (DellaGiustina et al. 2020). The boxes and numbers refer to areas examined in the designated figure.

Table 1. Spectral Parameters Examined

Spectral Parameter	Instrument	Wavelength range	Reference
Silicate stretching ratio (SR)[1]	OTES	10.0 - 12.4 µm (996 - 805 cm^{-1})	Hamilton et al., 2021
Silicate bending band depth (BBD)[2]	OTES	18.6 - 26.9 µm (537 - 372 cm^{-1})	Hamilton et al., 2021
Silicate stretching band depth (SBD)	OTES	10.7 - 17.2 µm (935 - 580 cm^{-1})	-
Thermal inertia	OTES	6 - 50 µm (1667 - 200 cm^{-1})	Rozitis et al., 2020
Equatorial station 3 (EQ3) Temperature	OTES	6 - 50 µm (1667 - 200 cm^{-1})	Rozitis et al., 2020
Bond albedo	OVIRS	0.4 - 2.5 µm (25000 - 4000 cm^{-1})	Li et al., 2021
2.74 µm Band depth	OVIRS	2.6 - 3.0 µm (3846 - 3333 cm^{-1})	Simon et al., 2020b
Normalized optical path length (NOPL)	OVIRS	2.6 - 3.3 µm (3846 - 3030 cm^{-1})	Praet et al., 2021
Effective single-particle absorption thickness (ESPAT)	OVIRS	2.6 - 3.3 µm (3846 - 3030 cm^{-1})	Praet et al., 2021
0.55 µm Reflectance	OVIRS	0.45 - 0.7 µm (22222 - 14286 cm^{-1})	Simon et al., 2020b
1.05 µm Band depth	OVIRS	0.88 - 1.27 µm (11364 - 7874 cm^{-1})	Simon et al., 2020a
1.4 µm Band depth	OVIRS	1.27 - 2.6 µm (7874 - 3846 cm^{-1})	Simon et al., 2020a
1.8 µm Band depth	OVIRS	1.27 - 2.6 µm (7874 - 3846 cm^{-1})	Simon et al., 2020a
2.3 µm Band depth	OVIRS	1.27 - 2.6 µm (7874 - 3846 cm^{-1})	Simon et al., 2020a
Spectral slope 0.5 to 1.5 µm	OVIRS	0.5 - 1.5 µm (20000 - 6667 cm^{-1})	Simon et al., 2020b
Band area 3.2 to 3.6 µm	OVIRS	3.2 - 3.6 µm (3125 - 2778 cm^{-1})	Simon et al., 2020b
Nanophase/Microphase Troilite	OVIRS	0.4 - 1.2 µm (25000 - 8333 cm^{-1})	Trang et al., 2021

Nanophase/Microphase Magnetite	OVIRS	0.4 - 1.2 µm (25000 - 8333 cm^{-1})	Trang et al., 2021
Nanophase/Microphase Iron	OVIRS	0.4 - 1.2 µm (25000 - 8333 cm^{-1})	Trang et al., 2021
Normal reflectance at 0.55 µm (*v*)	OCAMS[3]	0.52 - 0.58 µm (19231 - 17241 cm^{-1})	DellaGiustina et al., 2020
Normalized 0.85/0.55 µm *(x/v)* visible slope proxy	OCAMS[3]	0.52 - 0.89 µm (19231 - 11236 cm^{-1})	DellaGiustina et al., 2020
Normalized 0.47/0.55 µm *(b'/v)* near-UV slope proxy	OCAMS[3]	0.44 - 0.58 µm (22727 - 17241 cm^{-1})	DellaGiustina et al., 2020
Relative band strength at 0.7 µm (*w)*	OCAMS[3]	0.52 - 0.89 µm (19231 - 11236 cm^{-1})	DellaGiustina et al., 2020

[1]Referred to as R987/814 in Hamilton et al. (2021)
[2]Referred to as BD440 in Hamilton et al. (2021)
[3]Wavelength ranges for OCAMS MapCam bands are *b'*: 0.44 to 0.50 µm, *v*: 0.52 to 0.58 µm, *w*: 0.67 to 0.73 µm, and *x*: 0.82 to 0.89 µm. Wavelength ranges reported here are the minimum and maximum wavelengths among all bands used for the spectral parameter indicated.